Modeling Rectified Diffusion, with Application to Potential Bubble Growth in Marine Mammals

APPROVED BY

SUPERVISING COMMITTEE:

Dr. Mark F. Hamilton, Supervisor

Dr. Preston S. Wilson, Supervisor

Modeling Rectified Diffusion, with Application to Potential Bubble Growth in Marine Mammals

by

Adrian Larbi-Cherif, B.S.

THESIS

Presented to the Faculty of the Graduate School of
The University of Texas at Austin
in Partial Fulfillment
of the Requirements
for the Degree of

MASTER OF SCIENCE IN ENGINEERING

THE UNIVERSITY OF TEXAS AT AUSTIN
May 2009

Acknowledgments

I would like to express my deep gratitude for my advisor, Dr. Mark F. Hamilton, whose patience, guidance, and assistance during my graduate studies and writing of this thesis were invaluable.

I would like to thank Dr. Preston S. Wilson for reading my thesis and taking the time to hold Skype calls to enhance our conversations about his suggestions.

I would also like to thank Dr. Yurii A. Il'inskii for his hours of guidance and good nature while conducting this research.

In addition, thanks goes out to all of my fellow acoustics graduate students for our many conversations. Special thanks goes to the recently annointed Dr. Todd Hay for his advice and willingness to assist with any questions that were asked.

Last but not least, I would like to thank my family for their love and support throughout the years and for always believing that any endeavor in which I employ myself can be a successful one.

Modeling Rectified Diffusion, with Application to Potential Bubble Growth in Marine Mammals

Adrian Larbi-Cherif, M.S.
The University of Texas at Austin, 2009

Supervisors: Dr. Mark F. Hamilton
Dr. Preston S. Wilson

In this thesis, research by Crum and Mao [J. Acoust. Soc. Am. **99**, 2898–2907 (1996)] and Houser, Howard, and Ridgway [J. Theor. Biol. **213**, 183–195 (2001)] is extended by numerically investigating bubble growth (initial radius of 10 μm) during rectified diffusion for gas supersaturations up to 300% by using the Fyrillas-Szeri equation [J. Fluid Mech. **277**, 381–407 (1994)]. Bubble growth is simulated for a range of frequencies (100 Hz to 10 kHz), sound pressure levels (205 dB to 215 dB re 1 μPa), and gas supersaturations (150% to 300%). Simulations are presented for continuous and monofrequency excitation, repeated tone bursts, and pulsed frequency-modulated waveforms. The potential for bubble growth to occur in marine mammals is also considered. For the parameters considered, static diffusion becomes the dominant growth mechanism as supersaturation is increased, bubble growth is frequency independent away from bubble resonance, and bubble growth due to duty-cycle excitation can be modeled as an effective continuous

source with a reduced sound pressure level. A more accurate model of *in vivo* marine mammal tissue is required to determine if rectified diffusion can trigger bubble growth at the levels predicted in this thesis.

Table of Contents

Acknowledgments **iv**

Abstract **v**

List of Tables **ix**

List of Figures **x**

Chapter 1. Introduction **1**

Chapter 2. Review of Basic Equations **11**

2.1 Modeling Nitrogen Saturation in Marine Mammals 11
2.2 Static Diffusion: Epstein-Plesset Model 19
2.3 Rectified Diffusion 21
  2.3.1 Eller-Flynn Model 23
  2.3.2 Crum-Mao Model 24
  2.3.3 Fyrillas-Szeri Model 25
2.4 Modeling of Bubble Oscillation: Rayleigh-Plesset Equation . . 26

Chapter 3. Numerical Methods **29**

3.1 Numerical Integration of Rayleigh-Plesset Equation 29
3.2 Numerical Integration of Fyrillas-Szeri Equation 37
  3.2.1 Verification of Our Implementation of the Fyrillas-Szeri Equation 40

Chapter 4. Results **46**

4.1 Bubble Growth due to a Continuous Wave Source 47
  4.1.1 Instantaneous bubble radius 48
  4.1.2 Analysis of Bubble Growth for Continuous Insonification 52

4.2 Bubble growth due to Sonar Signals 64
    4.2.1 Monofrequency Sonar Source 66
    4.2.2 Bubble Growth for Frequency Sweeps 70
4.3 Modelling Bubble Growth in Stranded Marine Mammals . . . 74

Chapter 5. Conclusion **81**

Appendix **85**

Vita **94**

List of Tables

1.1 Comparison of underwater anthropogenic sound sources ordered by source level.[3] 2

4.1 Parameter values, which are based used by simulations in this thesis.[12] 48
4.2 $R_0(t_f)$ for $R_{00} = 10$ μm and $f = 1$ kHz. 56
4.3 Frequency versus time for model sonar signal in Fig. 4.15. . . . 72
4.4 Equilibrium radius at 30 s and 60 s for: $C_i(0)/C_0 = 1.5$, 2.0, and 3.0; SPL = 205 dB, 210 dB, and 215 dB; and $f = 1$ kHz. 80

List of Figures

1.1 Equilibrium bubble radius is shown versus time for a bubble exposed to different SPLs. The bubble radius is calculated using three different models: Crum,[16] Eller-Flynn,[15] and Fyrillas-Szeri.[17] The driving frequency is 500 Hz, the initial bubble radius is 10 μm, and the gas supersaturation is 113.5%. Except for an SPL = 220 dB, there are no significant differences between the three model predictions. Figure taken from Crum and Mao.[12] 8

2.1 (a) Dive profile and muscle tissue nitrogen tension for the bottlenose whale, and (b) ratio of muscle tissue nitrogen concentration and external partial pressure of nitrogen at a given depth.[14] 16

2.2 Results comparing nitrogen saturation levels in marine mammals for different dive profiles and modeling situations. On the left-hand side are calculations made by Houser et al.[14] estimating muscle tissue nitrogen tension in atmospheres and nitrogen saturation levels for a linear dive sequence. On the right-hand side are results from Ilinskii[21] for a similar, but sinusoidal dive profile. The results are in qualitative agreement. 18

2.3 Static dissolution of bubbles with (dashed curves) and without (solid curve) surface tension. The ratio f is gas concentration to saturation. The radius-time curve is plotted with respect to nondimensional variables x and ϵ, which are in terms of time and radius, respectively .[19] 21

2.4 Static growth of bubbles with (dashed curves) and without (solid curve) surface tension. The ratio f is gas concentration to saturation. The radius-time curve is plotted with respect to nondimensional variables x and ϵ, which are in terms of time and radius, respectively.[19] 21

3.1 $R(t)$ for (a) $R_0 = 10$ μm and (b) $R_0 = 200$ μm, driven at $f = 10$ kHz and an SPL = 215 dB. 35

3.2 Comparison of $R(t)$ for a bubble driven at $f = 10$ kHz, $R_0 = 0.1$ mm, and $p_a = 0.24$ MPa. (a) is Fig. 4.7 of Leighton,[13] (b) $R(t)$ from simulations of Eq. (2.12). 36

3.3 $R(t)$ for bubbles driven at $f = 10$ kHz and $R_0 = 10$ μm. The acoustic pressure function is shown in (a). $R(t)$ with $p_a = 0.24$ MPa is shown in (b), and $R(t)$ with $p_a =$ 0.14 MPa is shown in (c). 38

3.4 Plots comparing $R_0(t)$ for $f = 500$ Hz, and $C_i/C_0 = 2.0$. Plot (a) is reproduced from Crum and Mao[12] and contains data from Fyrillas and Szeri,[17] and (b) contains data from our implementation of Eq. (2.10). Plot (a) contains two curves for SPL = 220 dB, with each curve corresponding to a different model for rectified diffusion. The top curve for SPL = 220 dB was generated by Eq. (2.10) and the bottom curve was generated by the Eller-Flynn equation.[15] Plot (b) does not contain data for an SPL = 220 dB. In (b), the solid lines are in increasing SPL from bottom to top. Thus, the bottom solid line is for an SPL = 190 dB, and the top line is for SPL = 215 dB. . . . 42

3.5 Comparison of $R_0(t)$ between Eq. (2.10)[17] and the Ilinskii et al. model[18] for $f = 100$ Hz, $C_i/C_0 = 1.5$, and various SPLs. Plot (a) contains data for static diffusion, (b) SPL = 195 dB, (c) SPL = 205 dB, and (d) SPL = 215 dB. 43

3.6 Comparison of $R_0(t)$ between Eq. (2.10)[17] and the Ilinskii et al. model[18] for $f = 100$ Hz, $C_i/C_0 = 3.0$, and various SPLs. Plot (a) contains data for static diffusion, (b) SPL = 195 dB, (c) SPL = 205 dB, and (d) SPL = 215 dB. 45

4.1 Equilibrium radius versus time and instantaneous radius versus time for $R_{00} = 10$ μm, $f = 10$ kHz, and $C_i/C_0 = 3.0$. Plot (a) contains $R_0(t)$ data for static diffusion, and SPL = 205 dB, 210 dB, and 215 dB . The curves in (a) are arranged by increasing SPL. Plots (b)–(d), (e)–(g), and (h)–(j) show $R(t)$ at different times on the $R_0(t)$ curve for SPL = 205 dB, 210 dB, and 215 dB. 49

4.2 Simulation data of $R_0(t)$ plotted with Eq. 4.4 for $C = 1.98$, $R_{00} = 10$ μm, and $C_i/C_0 = 3.0$. 51

4.3 Plot (a) shows $\langle (R/R_0)^4 \rangle$ for a bubble with $R_{00} = 10$ μm, $f = 10$ kHz, SPL = 215 dB, and $C_i/C_0 = 3.0$. Plot (b) shows $\langle (R/R_0)^{4-3\eta} \rangle$, plot (c) is the inverse of Eq. (3.14), and (d) is the ratio of Eq. (3.4) to Eq. (3.3). Resonance occurs at $t = 30$ s . 53

4.4 Plot (a) shows $\langle (R/R_0)^4 \rangle$ for a bubble with $R_{00} = 10$ μm, $f = 1$ kHz, SPL = 215 dB, and $C_i/C_0 = 3.0$. Plot (b) shows $\langle (R/R_0)^{4-3\eta} \rangle$, plot (c) is the inverse of Eq. (3.14), and (d) is the ratio of Eq. (3.4) to Eq. (3.3). 54

4.5 Equilibrium radius versus time for $R_{00} = 10\ \mu$m and $f = 1$ kHz. The bubble is exposed to SPL = 205 dB, 210 dB, and 215 dB. Plot (a) shows $R_0(t)$ for $C_i/C_0 = 1.5$, and (b) shows $R_0(t)$ for $C_i/C_0 = 3.0$. Bubble growth increases with increasing SPL. . . 55

4.6 Percent increase in R_0 relative to static diffusion for $R_{00} = 10\ \mu$m and $f = 1$ kHz. Plot (a) shows the percent increase in R_0 for $C_i/C_0 = 1.5$ and (b) shows the percent increase in R_0 for $C_i/C_0 = 3.0$. 57

4.7 Equilibrium radius for a range of frequencies and gas supersaturations. In increasing order, the rows contain data for $f = 100$ Hz, 10 kHz, and 100 kHz. From left to right, the columns contain $R_0(t)$ for $C_i/C_0 = 1.5$ and 3.0. Each plot contains data for static diffusion and SPL = 205 dB, 210 dB, and 215 dB. 60

4.8 Equilibrium radius after 100 s versus driving frequency. Each plot contains data for SPL = 190 dB, 205 dB, 210 dB, and 215 dB. Plots (a)–(c) show $R_0(t_f)$ for $C_i/C_0 = 1.5$, 2.0, and 3.0 respectively. 61

4.9 Polytropic index as a function of R_0. The driving frequency ranges from 100 Hz to 100 kHz. 62

4.10 Equilibrium bubble radius versus time for several supersaturations, driving frequencies, and for static diffusion as well as SPL = 215 dB. From left to right, the columns show $R_0(t)$ for $f = 100$ Hz, 10 kHz, and 100 kHz. From top to down, the rows contain $R_0(t)$ for $C_i/C_0 = 1.5$, 2.0, and 3.0. Each plot contains $R_0(t)$ for static diffusion and SPL = 215 dB. 63

4.11 Percent increase in R_0 relative to static diffusion for $R_{00} = 10\ \mu$m and $f = 1$ kHz. Plot (a) shows the percent increase in R_0 with $C_i/C_0 = 1.5$ for static diffusion and (b) shows the percent increase in R_0 with $C_i/C_0 = 1.5$ for SPL = 215 dB. . 65

4.12 $R_0(t)$ for $f = 1$ kHz, SPL = 215 dB, $T_s = 10$ s, and DC = 10%, 20%, 50%, and 100%. The top curve in each plot is continuous insonification (DC = 100%) and the bottom curve is static diffusion. Plot (a) contains data for $C_i/C_0 = 1.5$ and plot (b) contains data for $C_i/C_0 = 3.0$. As C_i/C_0 increases, the periods of static diffusion and rectified diffusion are less apparent. . . . 67

4.13 Decibels down from 215 dB for a continuous wave source as a function of duty cycle for (a) $C_i/C_0 = 1.5$ and (b) $C_i/C_0 = 3.0$. The data points were obtained by matching $R_0(t_f)$ for a duty cycle to $R_0(t_f)$ at a lower SPL. The log relation is calculated using Eq. (4.10). The driving frequency is 1 kHz. 69

4.14 An HFM source for $f_1 = 20$ Hz, $f_2 = 100$ Hz, $T_\mathrm{w} = 0.25$ s, and $T = 1$ s. 71

4.15 Frequency versus time for two HFM sweeps and monofrequency excitation. Refer to Table 4.3 for parameter values. 72

4.16 Equilibrium radius for a bubble driven by the frequency signal in Fig. 4.15 at SPL = 215 dB, $C_i/C_0 = 1.5$, 2.0, and 3.0, $T_s = 12.5$ s, and DC = 20%. 73

4.17 Equilibrium radius versus time for a marine mammal that has surfaced with initial supersaturated levels of 1.5, 2.0, and 3.0. Bubble growth is caused by static diffusion. Equation (2.2) is used to calculate the nitrogen pressure in muscle tissue with $v_p = 0$ Pa/s. 77

4.18 Equilibrium radius versus time and $C_i(t)/C_0$ for $f = 1$ kHz, static diffusion and SPL = 205 dB, 210 dB, and 215 dB. The rows contain data for $C_i(0)/C_0 = 1.5$, 2.0, and 3.0. 79

Chapter 1

Introduction

Since the Industrial Revolution, the sources for generating anthropogenic (human-created) sound have greatly increased. Further technological development of sound sources increased the capacity for creating more intense sounds. Over the last few decades, the average noise levels in the world's oceans have increased at least tenfold.[1] Today, over 90% of sound in the ocean is due to commercial shipping.[2] A summary of underwater sources of sound is presented in Table 1.1. Of particular interest in this thesis is the generation of anthropogenic sound by man-made active sonar, in which an electromechanical or impulsive sonar projector creates bursts of acoustic waves that are used for vessel navigation and detection of objects underwater. The high source levels of sonar and other anthropogenic sources, as well as the increased level of ambient noise in the ocean, have generated concern over the impact that sound might have on aquatic life. Since the use of sound is vital for marine mammals, research has focused on the harmful effects that intense acoustic events could have on marine mammal behavior and physiology. The Marine Mammal Commision[1] states that the impact of anthropogenic sound can range from negligible to fatal.

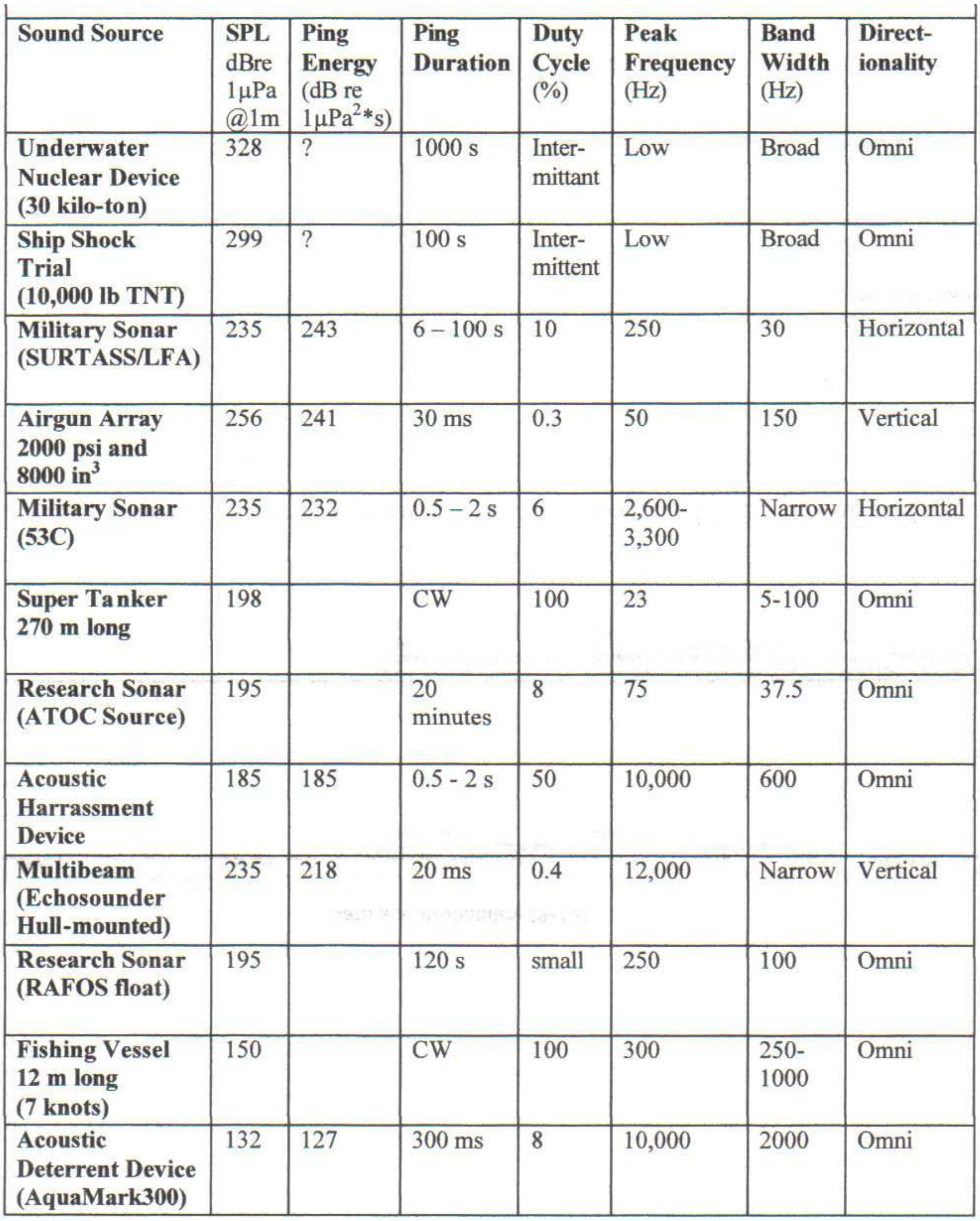

Sound Source	SPL dBre 1μPa @1m	Ping Energy (dB re 1μPa^2*s)	Ping Duration	Duty Cycle (%)	Peak Frequency (Hz)	Band Width (Hz)	Direct-ionality
Underwater Nuclear Device (30 kilo-ton)	328	?	1000 s	Inter-mittant	Low	Broad	Omni
Ship Shock Trial (10,000 lb TNT)	299	?	100 s	Inter-mittent	Low	Broad	Omni
Military Sonar (SURTASS/LFA)	235	243	6 – 100 s	10	250	30	Horizontal
Airgun Array 2000 psi and 8000 in^3	256	241	30 ms	0.3	50	150	Vertical
Military Sonar (53C)	235	232	0.5 – 2 s	6	2,600-3,300	Narrow	Horizontal
Super Tanker 270 m long	198		CW	100	23	5-100	Omni
Research Sonar (ATOC Source)	195		20 minutes	8	75	37.5	Omni
Acoustic Harrassment Device	185	185	0.5 - 2 s	50	10,000	600	Omni
Multibeam (Echosounder Hull-mounted)	235	218	20 ms	0.4	12,000	Narrow	Vertical
Research Sonar (RAFOS float)	195		120 s	small	250	100	Omni
Fishing Vessel 12 m long (7 knots)	150		CW	100	300	250-1000	Omni
Acoustic Deterrent Device (AquaMark300)	132	127	300 ms	8	10,000	2000	Omni

Table 1.1: Comparison of underwater anthropogenic sound sources ordered by source level.[3]

In 1996, during a military sonar exercise performed by the North Atlantic Treaty Organization (NATO), a mass stranding of 12 Cuvier's beaked whales occured in Greece. Gathering data on the history of Cuvier beaked whale strandings which occured locally and worldwide, Frantzis[4] hypothesized that the military manoevers could have caused or greatly influenced the mass stranding. During the stranding, NATO performed a sonar exercise using high-intensity (SPL $\geq$ 230 dB re 1 μPa), low-frequency (center frequencies ranged from 250 to 3,500 Hz) sonar.

In March 2000, a mass stranding of 17 cetaceans occured in the Bahamas during military sonar exercises. A joint investigation of the Bahamas stranding event was conducted by the National Oceanographic and Atmospheric Administration (NOAA) and the U.S. Navy.[5] The report concluded that the naval sonar was the most plausible source for the stranding. After performing necropsies on the seven dead cetaceans, the cetaceans "experienced some sort of acoustic or impulse trauma that led to their stranding and subsequent death."[5]

Since 2000, several additional stranding events have coincided with naval sonar exercises.[2] Researchers have concluded that beaked whales, especially Cuvier's beaked whales, are highly sensitive to mid-frequency active sonar.[5] The mechanisms that induce physical trauma and stranding of the beaked whales are currently unknown,[6,7] but research has been conducted on the possibility of the strandings occuring due to lesions and emboli caused by decompression sickness.[8–10]

In 2003, Jepson et al.[8] published necropsy results of 10 beaked whales (8 of which were Cuvier's beaked whales) that stranded in a period four hours after naval sonar exercises off the coast of the Canary Islands in 2002. The necropsies found trauma consistent with damage due to *in vivo* intravascular bubbles, and lesions that are "consistent with acute trauma due to *in vivo* bubble formation resulting from rapid decompression." Jepson et al.[8] hypothesize that it is possible for bubble growth by static diffusion to occur in marine mammals if nitrogen bubbles, which can be present in the supersaturated tissues of deep-diving marine mammals, are disturbed by a pressure field created by sonar. Static diffusion is discussed in Sec. 2.2. For this thesis, static diffusion refers to the process of gas exchange between a bubble and its surrounding liquid in the absence of an acoustic field.

In 1979, nitrogen supersaturation in dolphin muscle tissue was measured by Ridgway and Howard.[11] After a series of dives, it was estimated that one of the dolphins surfaced with a nitrogen supersaturation of 260%, providing evidence that dolphin tissue becomes supersaturated while diving. If a bubble is present in supersaturated tissue, growth can occur by static diffusion. Human divers strictly follow dive schedules that are designed to avoid bubble formation and decompression sickness. If supersaturated tissue is relieved of pressure too rapidly, excess nitrogen in the tissue can come out of solution and form bubbles. If a bubble grows to sufficient size, then it can induce decompression sickness, which can be fatal. Despite the observation that dolphin tissue can become supersaturated and that bubbles can be present, dolphins do not naturally get decompression sickness. The mechanism employed to prevent decompression sickness in dolphins is not known.[11]

In 1996, Crum and Mao[12] numerically investigated the potential for bubble growth to occur by rectified diffusion in order to investigate potential threats to human divers and marine mammals. Crum and Mao[12] found significant, rapid bubble growth due to rectified diffusion for SPLs of 210 dB and greater. This level of acoustic excitation is only present in the near vicinity of sonar projectors, hence marine mammals and divers would be safe from trauma induced by rectified diffusion as long as they are not in the immediate vicinity of sonar.

Rectified diffusion occurs when energy from a sound field transports dissolved gas from the surrounding liquid into a bubble. When a bubble is insonified by a harmonic source, it is driven into radial oscillation about its equilibrium radius. The equilibrim radius is the radius of the bubble when surface tension and atmospheric pressure act on the bubble. The bubble wall expands durng the negative phase of the acoustic source, and the bubble wall contracts during the positive phase of the acoustic source. If the gas pressure in the bubble becomes less than the pressure of dissolved gas in the adjacent liquid, then gas will flow from the liquid to the bubble. The opposite occurs during bubble wall compression and gas flows from the bubble into the liquid. The diffusion of gas between the bubble and liquid is proportional to the area of the transferral interface (i.e., the bubble wall), thus there will be a net flux of gas into the bubble. This is known as the area effect.[13] Rectified diffusion is further discussed in Sec. 2.3

Extending research that estimated dolphin tissue supersaturation,[11] Houser et al.[14] predicted nitrogen supersaturation in marine mammal muscle tissue after a dive sequence. Houser et al.[14] predict that marine mammals that make slow, deep dives while searching for food are more susceptible to bubble growth by rectified diffusion than marine mammals making shorter, shallower dives due to higher levels of accumulated nitrogen supersaturation. Nitrogen supersaturations estimated were greater than levels used by Crum and Mao.[12] The motivation for this thesis is to extend research by Crum and Mao[12] by investigating bubble growth due to rectified diffusion for nitrogen supersaturations predicted by Houser et al.[14]

Understanding bubble growth by static diffusion is a prerequisite to understanding bubble growth by rectified diffusion. In 1950, Epstein and Plesset[19] investigated the stability of gas bubbles in solution subject to static diffusion. They assumed that the bubble was immersed in an infinite liquid containing dissolved gas. Surface tension and atmospheric pressure act on the bubble. Due to surface tension, the pressure of gas in the bubble is greater than the pressure of the liquid surrounding the bubble wall. This additional pressure is called the Laplace pressure and it is inversely proportional to a bubble's radius. If the concentration of dissolved gas in the liquid is greater than the concentration of gas adjacent to the bubble wall, calculated using Henry's Law, then the bubble will grow. The bubble dissolves when the gas concentration adjacent to the bubble wall is greater than the gas concentration in the liquid. Refer to Sec. 2.2 for a more in-depth review of static diffusion.

The development of equations that estimate bubble growth due to rectified diffusion has a longstanding history.[15–18] The difficulty in calculating a bubble's radius subject to rectified diffusion is that the moving boundary of the bubble wall creates concentration gradients and temperature gradients at the bubble wall, thus coupling the motion of the bubble wall to the diffusion of gas concentration and heat diffusion. Also, the equation of motion, the Rayleigh-Plesset equation, is dependent upon the pressure of the gas inside the bubble. As dissolved gas is exchanged between the bubble and the liquid, the pressure of the gas inside the bubble changes.[13] Rectified diffusion is reviewed in Sec. 2.3, and the Rayleigh-Plesset equation is reviewed in Sec. 2.4.

Now, we will refer back to bubble growth calculations made by Crum and Mao[12] to investigate diver and marine mammal safety. Crum and Mao[12] calculated bubble growth using three rectified diffusion models: the Crum model,[16] the Eller-Flynn model,[15] and the Fyrillas-Szeri model.[17] Each model is discussed in Sec. 2.3. The Crum model, Eller-Flynn model, and Fyrillas-Szeri model predict similar bubble growth rates at drive levels up to 210 dB, but predict significantly different bubble growth rates at 220 dB, as shown in Fig. 1.1. At the time of publication by Crum and Mao,[12] the Fyrillas-Szeri model was the most rigorous treatment of the rectified diffusion.[12,17]

A more exact model of rectified diffusion has been implemented by Ilinskii et al.[18] A large Péclet number was assumed in previous models. The Péclet number is a ratio of advection (transport of a quantity due to motion of

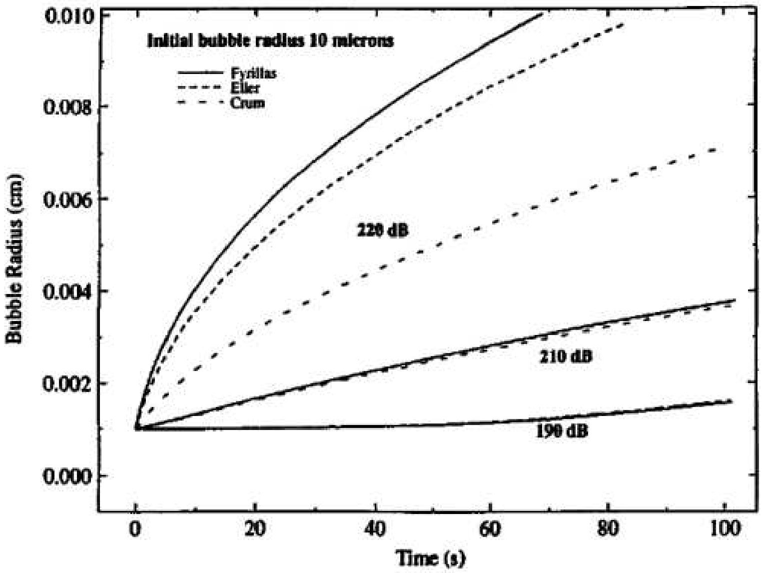

Figure 1.1: Equilibrium bubble radius is shown versus time for a bubble exposed to different SPLs. The bubble radius is calculated using three different models: Crum,[16] Eller-Flynn,[15] and Fyrillas-Szeri.[17] The driving frequency is 500 Hz, the initial bubble radius is 10 μm, and the gas supersaturation is 113.5%. Except for an SPL = 220 dB, there are no significant differences between the three model predictions. Figure taken from Crum and Mao.[12]

the medium) to static diffusion (transport due to concentration gradients). For diffusion of a gas in a solution, a large Péclet number implies that the majority of gas transport occurs due to advection than due to static diffusion. Ilinskii et al.[18] conclude that bubble growth in previous models is underestimated by 10%–20% because of the assumption that the gas concentration in the liquid is given by a constant equilibrium radius. The underestimations are increased when high supersaturation levels (250%–300%) drive initial static diffusion. Ilinskii et al.[18] consider several factors that are not accounted for in previous rectified diffusion models:[15–17] the compressibility of the liquid surrounding the bubble, temperature gradients in the liquid near the bubble, and heat conduction within the bubble. The model takes significantly longer to run than the Fyrillas-Szeri model.

Due to the significant computation time, and the fairly small difference from predictions by the Ilinski model, the Fyrillas-Szeri model is used in this work. The effect of gas concentration, acoustic excitation amplitude, and excitation frequency were studied. Continuous wave sources, monfrequency sonar sources, and a Hyperbolic Frequency Modulation (HFM) signal were used to excite the bubble. Comparisons of results from the Fyrillas-Szeri model[17] were made with the model of Ilinskii et al.[18] for a subset of the parameter space. The possible effects of bubble growth due to rectified diffusion in marine mammals is discussed. The reader is advised that the rectified diffusion models used here pertains to an air bubble growing or dissolving in a liquid environment of infinite extent, and that this environment does not necessarily represent the environment of a bubble in marine mammal tissue.

In Chapter 2, the model equations used in this thesis are reviewed, including those for modeling gas concentration in dolphins,[11,14] bubble growth by rectified diffusion, and the equation of motion. Chapter 3 provides an overview of the techniques utilized to numerically integrate the Rayleigh-Plesset equation[12] and the Fyrillas-Szeri equation.[17] Chapter 4 presents results from simulations using continuous wave sources and sonar signals, as well as a simulation of bubble growth and dissolution in a marine mammal that stays at the surface for an extended period of time. In Chapter 5, conclusions are drawn about the possibility of rectified diffusion severely affecting marine mammals.

Chapter 2

Review of Basic Equations

In this chapter, the theoretical groundwork is laid to model rectified diffusion. Two coupled equations will be used to determine the bubble's equilibrium radius as gas is transferred between the bubble and the surrounding liquid. The medium of interest is a solution of seawater and dissolved gas at 20°C. To model the problem accurately, an equation of motion for the bubble wall is needed, as well as a diffusion equation for the concentration of dissolved gas in the liquid.

In Sec. 2.1, previous research involving modeling of nitrogen saturation in marine mammals is reviewed. Static diffusion and rectified diffusion models are reviewed in Sec. 2.2. In Sec. 2.3, the Rayleigh-Plesset equation, an equation of motion, is introduced.

2.1 Modeling Nitrogen Saturation in Marine Mammals

In 1979, Ridgway and Howard[11] conducted a study to observe intramuscular nitrogen tension (i.e., partial pressure due to nitrogen gas) in bottlenose dolphins after a dive series. Motivated by previous studies, Ridgway and Howard were investigating if pulmonary collapse can prevent decompression illness in marine mammals during deep dives (dives > 70 m). Pulmonary collapse is defined as the partial or total loss of air in the lungs.[20] The research involved two dolphins, Blue and Brown, who each completed a dive series over an hour. The dolphins dove to a depth of 100 m, pushed a switch at the end of a dive cable, returned to the surface, and then waited approximately 45 seconds before diving again. The researchers determined an ascent/descent rate, defined as the average change of depth per unit time for a dolphin to complete a dive and return. After the dive series, nitrogen washout and intramuscular nitrogen tension was measured using a mass spectrometer probe which was inserted transcutaneously into the dorsal epaxial muscle tissue. Nitrogen tension is equivalent to the partial pressure of a gas.

It was found through linear regression that after the dive series, Blue had an intramuscular tension of 1600 mmHg (260% supersaturation) and Brown had an intramuscular tension of 1300 mmHg (212% supersaturation). Also of interest was the nitrogen washout rate, from which the nitrogen half-time for muscle tissues were derived. The nitrogen half-time, t_w, was 5.2 min for Blue and 6.6 min for Brown, leading to a mean half-time of 5.9 min. Half-time for nitrogen washout is the amount of time it takes for muscle tissue to intake or release nitrogen to half of its saturation value.[11] The researchers assumed an equal half-time for nitrogen washin and washout, implying that the muscle tissues intake excess nitrogen at the same rate as they expel excess gas.

To model the intramuscular tension,[11] the following differential equation is used:

$$\frac{dp_n}{dt} = -\frac{p_n - p(t)}{\tau_w}, \tag{2.1}$$

where p_n is intramuscular nitrogen tension, $p(t)$ is the external partial pressure of nitrogen, and $\tau_w = t_w / \ln 2$. The particular solution of Eq. (2.1) is[21]

$$p_n = p_{ag} + v_p \left(t - \tau_w\right) + e^{-t/\tau_w} \left(p_0 - p_{ag} + v_p \tau_w\right), \tag{2.2}$$

where p_{ag} is the initial pressure of alveolar nitrogen, v_p is the change in nitrogen pressure per unit time, t is time, and p_0 is the initial partial pressure due to nitrogen, which is comprised of hydrostatic pressure and atmospheric pressure. It is important to define the significance of partial pressure in this problem. Air is normally comprised of 78% nitrogen and 21% oxygen. Since oxygen is metabolized by aerobic organisms, the gas pressure of interest becomes that of the non-metabolized nitrogen gas.[22]

Ridgway and Howard[11] found that Eq. (2.1) overestimated nitrogen supersaturation levels because Eq. (2.1) does not account for total pulmonary collapse, whichoccurs in dolphins to enable longer dive times. When pulmonary collapse occurs, oxygen stored in the blood is used almost entirely by the heart and brain. Also, when the lungs totally collapse the dolphins do not exchange gas with the surrounding medium, and thus the nitrogen concentration remains constant while the lungs are totally collapsed. Total pulmonary collapse was predicted to occur at 65 m in Brown and 70 m in Blue. The paper concludes that bottlenose dolphins are not immune to decompression sickness due to high nitrogen supersaturation levels measured at the end of the dive series, but the mechanisms utilized to manage excess nitrogen without suffering from decompression sickness were not apparent.

There has been increasing concern during the last fifteen years about anthropogenic sound in the ocean and its effect on marine mammal life. Following several stranding events after naval sonar exercises, it has been speculated that high-amplitude, active sonar might adversely affect cetacean behavior and/or physiology.[4–6,8] Concerned by this, in 2001 Houser, Howard, and Ridgway[14] modeled gas pressure in three cetacean species: the bottlenose dolphin, the bottlenose whale (a beaked whale), and the blue whale (a baleen whale). The research was an extension of previous work conducted by Ridgway[11] and also in response to a paper published by Crum and Mao,[12] which investigated rectified diffusion potentially affecting divers and marine mammals. Houser et al.[14] were investigating to see if intramuscular nitrogen saturation levels would be sufficient to cause growth of gas bubbles if activated by insonification. The bubble growth could occur either by rectified or static diffusion.

Equation (2.1) was used to model nitrogen saturation levels in marine mammal tissue.[11] Following Ridgway and Howard[11] a washout time of 5.9 min was used, and pulmonary collapse was predicted to occur at 70 m for all three cetacean species. Thus, below a depth of 70 m, nitrogen supersaturation levels remained constant. Specific data for nitrogen washin/washout times and depth of pulmonary collapse were only available for the bottlenose dolphin.[14] To model the intramuscular nitrogen tension, each cetacean 'performed' a series of dives. Dive sequences, dive depths, and dive speeds were used for marine mammals based on recorded data from tagged animals of that species. The dive series used for the dolphin was similar to one previously utilized by Ridgway.[11] Nitrogen pressure was calculated at each point in the dive. Since the dive series and dive behavior used is different for each species, the supersaturation levels will vary between the species.[14]

It was predicted that each species acquired an intramuscular nitrogen tension greater than 200% of its surface value. The bottlenose whale acquired the highest saturation levels, surpassing 300% during its dive series.[14] Figure 2.1 illustrates the muscle tissue nitrogen tension of a bottlenose whale during a dive series. In Fig. 2.1(a), the darker plot is the partial pressure of nitrogen as a function of time, and the lighter plot is the dive profile of the bottlenose whale. In this dive series, the bottlenose whale did two shorter dives to a depth of 100 m, and then a longer dive to a depth of 1060 m. Figure 2.1(b) shows the ratio of instantaneous muscle tissue nitrogen concentration to external nitrogen concentration at each point in the dive. One can see in Fig. 2.1(a) the fluctuating nature of nitrogen tension during a dive. During the rest period, the nitrogen concentration in the tissue will decrease because it is supersaturated relative to the nitrogen content of atmospheric air.

Of concern to the Houser et al.,[14] if a bubble nucleus is perturbed by a pressure fluctuation (e.g., an acoustic field) at these saturation levels, static diffusion can occur rapidly. Moreover, this growth may be augmented by rectified diffusion if the marine mammal is insonified by a sonar signal.[12]

A review of research by Ridgway and Howard[11] and Houser et al.[14] was

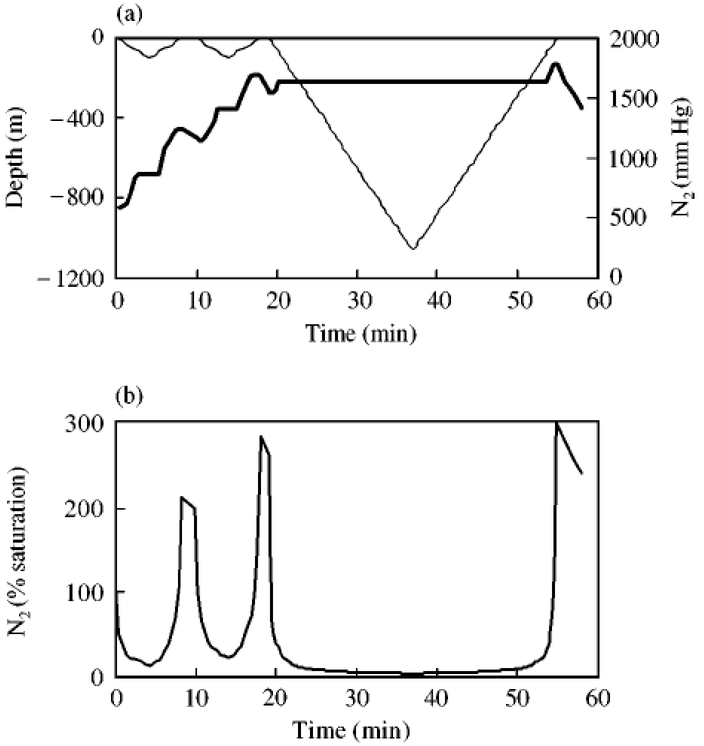

Figure 2.1: (a) Dive profile and muscle tissue nitrogen tension for the bottlenose whale, and (b) ratio of muscle tissue nitrogen concentration and external partial pressure of nitrogen at a given depth.[14]

conducted by Ilinskii.[21] To model the dive profile, Ilinskii used a sinusoidal dive profile and derived a simple analytic solution for the nitrogen saturation levels. Setting the external pressure to $p(t) = p_0 + \frac{1}{2}\rho g d\,(1 - \cos\omega t)$, where $\omega = 2\pi/T$ and T is the dive period, he found that the partial pressure of nitrogen as a function of time is[21]

$$p_n = p_0 + \frac{1}{2}\rho g d\left(1 - e^{-t/\tau_w}\right) - \mathrm{Re}\left[\frac{1}{2}\rho g d \frac{e^{j\omega t} - e^{-t/\tau_w}}{1 + j\omega\tau_w}\right] \tag{2.3}$$

$$\rightarrow \frac{1}{2}\rho g d\left[1 - \frac{\cos(\omega t - \arctan\omega\tau_w)}{\sqrt{1 + (\omega\tau_w)^2}}\right]\ ,\ t \gg \tau_w \tag{2.4}$$

Ilinskii used Eq. (2.3) to compare with linear dive profile results for a bottlenose dolphin from research performed by Houser et al.[14] Two key differences between the two analyses are that Ilinskii did not account for lung collapse and did not have a rest period. Because of this setup, Ilinskii's calculations[21] of intramuscular nitrogen are much higher than results by Houser et al.[14] By not accounting for lung collapse, the dolphin will be intaking the most dense air during the dive cycle and thus will greatly increase the nitrogen concentration in the tissue. By not having a rest period, the dolphin has no time to release the excess nitrogen inhaled during the dive and further increases the level of supersaturation. The reader can refer to Fig. 2.2, which is similar to Fig. 2.1. In the first column, results from Houser et al.[14] are presented, and the second column analysis by Ilinskii is presented.

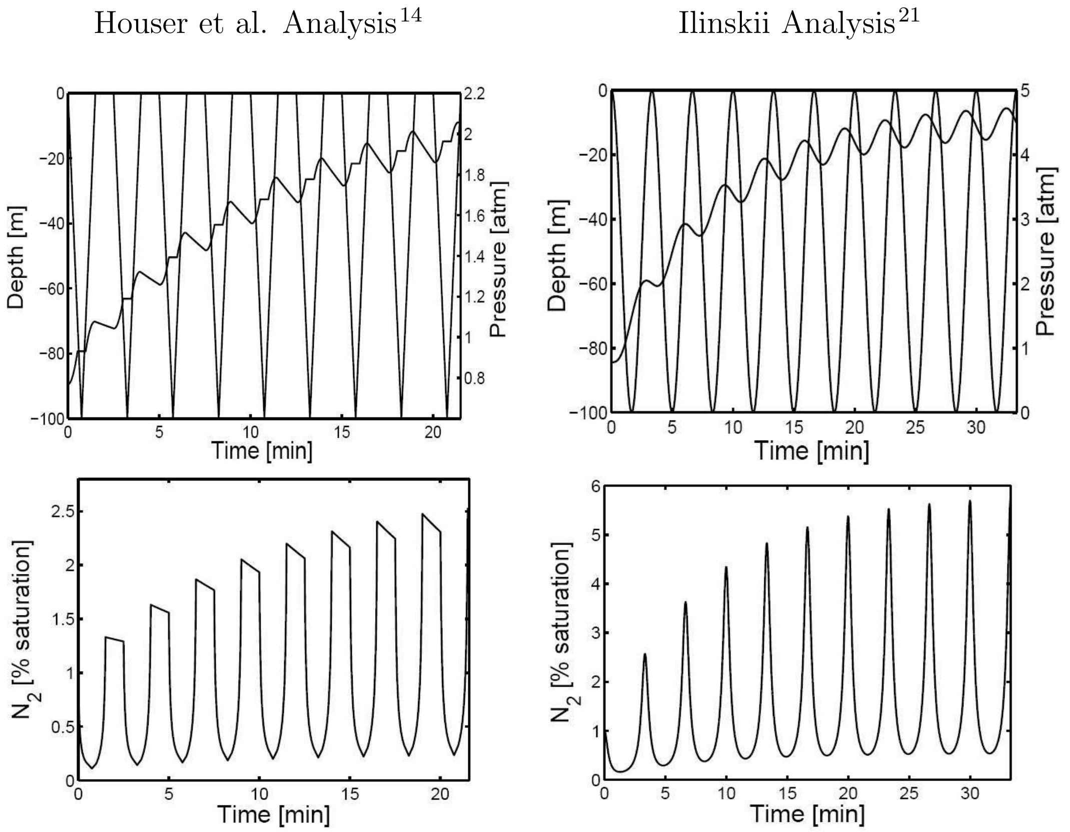

Houser et al. Analysis[14]

Ilinskii Analysis[21]

Figure 2.2: Results comparing nitrogen saturation levels in marine mammals for different dive profiles and modeling situations. On the left-hand side are calculations made by Houser et al.[14] estimating muscle tissue nitrogen tension in atmospheres and nitrogen saturation levels for a linear dive sequence. On the right-hand side are results from Ilinskii[21] for a similar, but sinusoidal dive profile. The results are in qualitative agreement.

2.2 Static Diffusion: Epstein-Plesset Model

In 1950, Epstein and Plesset[19] published a paper detailing their theoretical model for increase or decrease in the size of a spherical bubble in a liquid-gas solution. The authors predicted growth or dissolution as a function of the dissolved gas concentration gradient between the bubble wall and at some point far from the bubble. In their analysis, a bubble of initial equilibrium radius R_0 is located in an infinite, incompressible fluid. Spherical symmetry is assumed, with the origin of the coordinate system coinciding with the center of the bubble. The bubble neither translates nor oscillates, but it can grow or dissolve. The temperature of the liquid-gas solution is held constant and thus acts as a heat reservoir. Initially, the fluid has a gas concentration of C_i. At the bubble wall, the concentration C_R is determined by Henry's law, which states that the concentration of gas in solution is proportional to the partial pressure of the gas adjacent to the solution. The pressure of the gas in the bubble is due to an ambient, hydrostatic pressure and surface tension. Thus,

$$C_R = \frac{P_0 + 2\sigma/R_0}{H_d} = C_0 \left(1 + \frac{2\sigma}{P_0 R_0}\right), \tag{2.5}$$

where P_0 is the hydrostatic pressure, σ is the surface tension, H_d is Henry's constant, and C_0 is the gas concentration due to hydrostatic pressure.

To describe the transportation of gas throughout the medium, Fick's law of mass transfer was used:[13]

$$\frac{\partial C}{\partial t} + v_r \frac{\partial C}{\partial r} = D \left(\frac{\partial^2 C}{\partial r^2} + \frac{2}{r}\frac{\partial C}{\partial r}\right), \tag{2.6}$$

where v_r is the radial velocity of the fluid at a given point r, and D is the gas diffusivity constant for the gas in the liquid. This equation can be simplified by neglecting the contribution of convection-enhanced diffusion. More specifically, $v_r \frac{\partial C}{\partial r} \approx 0$ since $v_r \approx 0$.[13] This is very reasonable for two reasons. First, it follows from the continuity equation that the radial velocity of the fluid is inversely proportional to the square of the distance from the origin, or $v_r = (R_0/r)^2 \dot{R}_0$. Second, and most important, bubble sizes are chosen for static diffusion to be a slow process. If the bubble is sufficiently small, then surface tension can cause rapid dissolution of the bubble.

Epstein and Plesset[19] found that the bubble would grow when $C_i > C_R$ and would dissolve when $C_i < C_R$. If $C_i = C_R$, no diffusion would occur because there would not be a concentration gradient in the fluid. They derived the following equation for the rate of change of the equilibrium radius:

$$\frac{dR_0}{dt} = \frac{Dd}{R_0}\left[\frac{C_i}{C_0} - \left(1 + \frac{2\sigma}{p_0 R_0}\right)\right]\left(1 + \frac{4\sigma}{3R_0 P_0}\right)^{-1}\left(1 + \frac{R_0}{\sqrt{\pi D t}}\right), \qquad (2.7)$$

where $d = RTC_0/P_0$, R is the universal gas constant, and T is the equilibrium temperature. In Eq. (2.7), one can readily observe growth trends in a bubble subject to static diffusion. The only term in the equation that can be negative is the term containing gas concentration ratios. As stated above, if $C_i < C_R$ the bubble will eventually dissolve because the growth rate will become negative (refer to Eq. (2.7) for the definition of C_R). The ratio C_i/C_0 is constant and will not affect the rate of change of the bubble radius as the bubble changes size. Also, as R_0 decreases, the pressure due to surface tension increases and further enhances the dissolution rate. If $C_i > C_R$, then the bubble will grow, and surface tension will decrease over time. To illustrate the above equation, refer to Fig. 2.3(a) and Fig. 2.3(b). In the figure, $f = C_i/C_R$, $\epsilon = R_0/R_{00}$, where R_{00} is the initial equilibrium radius, and χ is the nondimensional time.

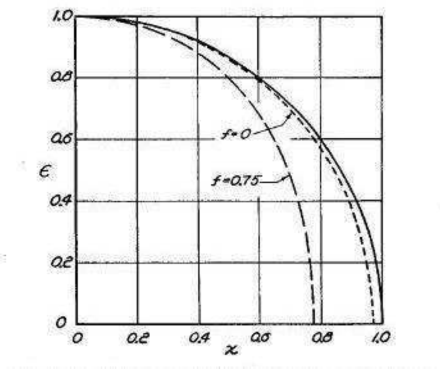

Figure 2.3: Static dissolution of bubbles with (dashed curves) and without (solid curve) surface tension. The ratio f is gas concentration to saturation. The radius-time curve is plotted with respect to nondimensional variables x and ϵ, which are in terms of time and radius, respectively .[19]

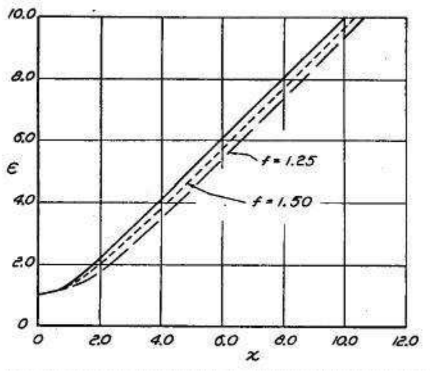

Figure 2.4: Static growth of bubbles with (dashed curves) and without (solid curve) surface tension. The ratio f is gas concentration to saturation. The radius-time curve is plotted with respect to nondimensional variables x and ϵ, which are in terms of time and radius, respectively.[19]

2.3 Rectified Diffusion

Diffusion can be enhanced if the bubble is in a sound field. The pressure fluctuations caused by acoustic waves create radial oscillations of the bubble wall, which in turn create a velocity field in the incompressible liquid. Due to the bubble oscillations, the convection term in the diffusion equation can no longer be neglected.[13] Also, oscillations of the bubble wall change the gas concentration in the bubble and thus change the gas concentration at the bubble wall. These two factors couple the diffusion equation to an equation of motion for the bubble wall, namely the Rayleigh-Plesset equation.

As the bubble oscillates, heat will be transferred between the liquid and the bubble. When the bubble contracts, its temperature will increase and become greater than the temperature of the liquid adjacent to the bubble wall, and heat will tend to diffuse out of the bubble. The opposite occurs when the bubble expands. To account for heat transfer between the bubble and the fluid, it is generally assumed that the temperature of the liquid is constant and acts as a heat reservoir for the bubble. Thus, heat exchange between the bubble and liquid will not affect gas transport in the liquid because the temperature of the liquid is not changing, which would then change the random motions of the water molecules and dissolved gas molecules.

Bubbles of interest in this thesis are small compared to an acoustic wavelength, and therefore the pressure across the surface of the bubble will be spatially constant. This in turn leads to treating all thermodynamic variables (temperature, gas concentration, etc.) within the bubble as spatially invariant.[15] In the following subsections, the Eller-Flynn model,[15] Crum-Mao model,[12] and Fyrillas-Szeri model[17] will be discussed to illustrate their respective approaches on modeling rectified diffusion.

2.3.1 Eller-Flynn Model

To simplify calculating mass flux into a bubble due to rectified diffusion, Eller and Flynn[15] considered motion of the bubble wall and diffusion of gas in the liquid as two separate problems. This assumption is valid when the time scale for diffusion is much longer than the time for a single bubble oscillation,[13,15] which is equivalent to an acoustic cycle when the transients of a forced oscillation have negligible affects. With this assumption, Eller and Flynn solved the Rayleigh-Plesset equation numerically. This simplification is termed the "high-frequency" approximation, and is valid for $\omega \gg D/R_0^2$, where D is the diffusion constant for the gas in a liquid, and R_0 is the equilibrium radius of the bubble. The equilibrium radius is defined as the radius of the undisturbed, unforced bubble.[13] The reader should keep in mind that although the bubble is in "equilibrium" and is not being driven, it may still be changing size due to the excess pressure in the bubble because of surface tension. In effect, the equilibrium radius of a bubble is an unstable equilibrium.

To find the net change in bubble radius over a time period of forced oscillations, time averages are calculated based on the ratio of instantaneous radius to equilibrium radius. The time averages then can be used in an equation tracking the rate of change of the bubble radius:[12,15]

$$\begin{aligned}\frac{dR_0}{dt} =& \frac{Dd}{R_0}\left[\left\langle \frac{R}{R_0}\right\rangle + R_0\left(\frac{1}{\pi D t}\left\langle\left(\frac{R}{R_0}\right)^4\right\rangle\right)^{1/2}\right] \\ & \left(1+\frac{4\sigma}{3R_0P_0}\right)^{-1}\left(\frac{C_i}{C_0} - \left\langle\left(\frac{R}{R_0}\right)^4\frac{P_g}{P_0}\right\rangle\left\langle\left(\frac{R}{R_0}\right)^4\right\rangle^{-1}\right), \qquad (2.8)\end{aligned}$$

where $d = RTC_0/p_0$, R is the universal gas constant, T is the equilibrium temperature, C_0 is the saturation concentration determined by Henry's law, C_i is the gas concentration far from the bubble, and σ is the surface tension. Concentration is measured in molar density. If bubble oscillations about the equilibrium radius are negligible (similar to a bubble at rest during static diffusion), then the time averages in Eq. (2.8) are approximately 1. This approximation yields the equation for static diffusion, Eq. (2.7), derived by Epstein and Plesset.[19]

2.3.2 Crum-Mao Model

Crum and Mao[12] simplified the analysis made by Eller and Flynn by assuming that the bubble dynamics can be expressed as a second order expansion in terms of the acoustic pressure. This approximation is valid for acoustic pressure amplitudes less than 0.05 MPa ($\approx$ 185 dB).[23] Under these pressure constraints, the pressure of the gas inside the bubble is approximately constant during an oscillation since the pressure fluctuations due to surface tension will be small compared to the ambient pressure. Crum's analysis replaced the time-averages in the Eller-Flynn formulation with expressions independent of the instantaneous bubble radius. With this substitution, the Rayleigh-Plesset equation does not need to be evaluated, and only the equation modeling the change of the equilibrium radius is evaluated.[16,23] The ratio evaluated by Crum[16,23] and also by Crum and Mao[12] to approximate the ratio of instantaneous radius to equilibrium radius is

$$\frac{R}{R_0} = 1 + \alpha \left(\frac{p_a}{p_0} \right) \cos(\omega t + \delta) + K \alpha^2 \left(\frac{p_a}{p_0} \right)^2 + \ldots , \tag{2.9}$$

where α, δ, and K are parameters defined by Crum.

2.3.3 Fyrillas-Szeri Model

Previous models of rectified diffusion only account for diffusion in a thin layer of liquid adjacent to the bubble wall.[17] But, the diffusion layer grows as $\sqrt{t}$ and thus this approximation is valid for only a short period of time. This limitation is noted by Eller and Flynn in their analyses.[15,17] If it is assumed that diffusion of gas occurs only in a thin layer adjacent to the bubble wall, then the rectified diffusion model underestimates bubble growth for acoustic pressure amplitudes greater than the threshold for rectified diffusion.

In the analysis by Fyrillas and Szeri,[17] the process of rectified diffusion is separated into two parts: the "smooth" problem, and the "oscillatory" problem. Each problem has its own set of boundary conditions and determines the concentration field in the liquid such that $C = C_{\text{sm}} + C_{\text{osc}}$. The oscillatory part of the problem deals with the rapid pressure fluctuations on the bubble wall due to the acoustic field. The oscillating pressure induces an oscillating gas concentration at the bubble wall. The net transfer of gas due to the oscillatory problem is negligible.[17] The smooth problem deals with convection-enhanced diffusion which occurs over a much longer time period than a bubble oscillation and is valid for all time. The expression for the bubble radius is[17]

$$\begin{aligned}\frac{dR_0}{dt} =& \frac{Dd}{R_0}\left(1+\frac{4\sigma}{3R_0P_\infty}\right)^{-1}\left(\frac{C_i}{C_0}-\frac{(1+2\sigma/R_0P_\infty)\left\langle (R/R_0)^{4-3\eta}\right\rangle}{\left\langle (R/R_0)^4\right\rangle}\right)\\ &\times\left(\int_0^\infty \frac{dx}{\left\langle \left[3x+(R/R_0)^3\right]^{\frac{4}{3}}\right\rangle}\right)^{-1}. \end{aligned} \tag{2.10}$$

2.4 Modeling of Bubble Oscillation: Rayleigh-Plesset Equation

The Rayleigh-Plesset equation is a second-order, nonlinear differential equation that is used to estimate the instantaneous bubble radius. For our study, bubble sizes are on the order of microns. It is assumed that the bubble is an incompressible liquid and has several pressure sources acting on it (e.g., atmospheric pressure, hydrostatic pressure, acoustic field, surface tension, etc.). Body forces such as gravity are not accounted for in the Rayleigh-Plesset equation. The fundamental form of the Rayleigh-Plesset equation is

$$R\ddot{R}+\frac{3}{2}\dot{R}^2=\frac{p_L-p_\infty}{\rho}, \tag{2.11}$$

where R is the bubble radius, ρ is the density of the liquid, p_L is the pressure in the liquid adjacent to the bubble wall, and p_∞ is the pressure field far from the bubble. Spatially uniform thermodynamic conditions (i.e., pressure, temperature, concentration) exist within the bubble. The number of gas molecules within the bubble remains constant throughout calculations.[13]

Suppose that at $t = 0$, a bubble of radius R_0 is subject to a unifrom pressure p_0 which is present throughout the liquid. For $t > 0$, far away, sound waves are generated and are propagating towards the bubble. Since the bubble is in an incompressible medium, the wavelength of the driving sound wave is much larger than the bubble radius.[24] The pressure far away from the bubble becomes $p_\infty = p_0 + p_a(t)$, where p_0 is the atmospheric pressure and $p_a(t)$ is the acoustic pressure. The bubble is also subject to thermal, viscous, and radiation damping. To account for damping, the approach used by Devin and later Eller will be utilized.[25] This approach is valid for small-amplitude, radial oscillations about the equilibrium radius of the bubble. This allows for the bubble to be modeled as a forced harmonic oscillator.[26] The form of the Rayleigh-Plesset equation to be used in this paper is

$$\begin{aligned} R\ddot{R} + \frac{3\dot{R}^2}{2} =& \frac{1}{\rho}\Bigg[\left(p_0 + \frac{2\sigma}{R_0}\right)\left(\frac{R_0}{R}\right)^{3\eta} - p_0 - \frac{2\sigma}{R} \\ &+ p_a \sin(\omega t) - \frac{4\mu}{R}\dot{R} - \rho R_0 \frac{\omega_0^2}{\omega}\left(b_r + b_t\right)\dot{R}\Bigg], \end{aligned} \tag{2.12}$$

where σ is the surface tension, ω is the angular frequency of the acoustic source, and μ is the coefficient of shear viscosity. The angular resonance frequency of the bubble ω_0 is defined by

$$\omega_0^2 = \frac{1}{\rho R_0^2}\left[3\eta\left(p_0 + \frac{2\sigma}{R_0}\right) - \frac{2\sigma}{R_0}\right]. \tag{2.13}$$

The expression for the resonance frequency is

$$f_0 = \frac{1}{R_0}\sqrt{\frac{3\eta}{\rho}\left(p_0 + \frac{2\sigma}{R_0}\right) - \frac{2\sigma}{\rho R_0}}. \tag{2.14}$$

The polytropic index η is defined by

$$\eta = \gamma\left(1 + b_t^2\right)\left[1 + \frac{3\left(\gamma - 1\right)}{X}\left(\frac{S_{-}}{C_{-}}\right)\right]^{-1}, \tag{2.15}$$

where

$$S_{\pm} = \sinh X \pm \sin X, \tag{2.16}$$

$$C_{-} = \cosh X - \cos X, \tag{2.17}$$

$$X = R_0 \left(2\omega / D_1\right)^{1/2}, \tag{2.18}$$

and D_1 is the thermal diffusion constant of the gas. The thermal damping constant is

$$b_t = 3\left(\gamma - 1\right)\left[\frac{X S_{+} - 2C_{-}}{X^2 C_{-} + 3\left(\gamma - 1\right) X S_{-}}\right]. \tag{2.19}$$

The radiation damping constant b_r is given by

$$b_r = \frac{\rho R_0^3 \omega^3}{3\eta\left(p_0 + 2\sigma/R_0\right) c \left\{1 - 2\sigma / \left[3\eta R_0 \left(p_0 + 2\sigma/R_0\right)\right]\right\}}, \tag{2.20}$$

where c is the speed of sound in liquid.

In Chapter 3, the numerical techniques involved in integrating the equation of motion and diffusion equations will be discussed. The chapter provides information on nondimensionalization of the differential equations, numerical integration techniques, sequentialization of integration, and other numerical methods needed to analyze data.

Chapter 3

Numerical Methods

In this chapter, the algorithms used to calculate the equilibrium bubble radius during rectified diffusion are outlined. First, the numerical algorithm for the Rayleigh-Plesset equation, Eq. (2.12), is discussed. Then, numerical integration of the Fyrillas-Szeri equation, Eq. (2.10), is presented. Both Eq. (2.10) and Eq. (2.12) are integrated using a fourth-order, adaptive step size Runge-Kutta algorithm.[27] In each section, the validity of the bubble growth model is discussed.

3.1 Numerical Integration of Rayleigh-Plesset Equation

Numerical integration of Eq. (2.12) is performed using a fourth-order, adaptive step size Runge-Kutta Method.[27] Solution of Eq. (2.12) yields the instantaneous bubble radius as a function of time, $R(t)$. Viscosity, surface tension, and an acoustic field (typically a time-harmonic source of frequency f) act on the bubble. The equilibrium radius R_0 is constant during integration. During integration of Eq. (2.12), the time averages $\langle (R/R_0)^4 \rangle$ and $\langle (R/R_0)^{4-3\eta} \rangle$ are calculated over a period T for the forcing frequency f, which are necessary for integration of Eq. (2.10).

To use the Runge-Kutta method, differential equations and the respective initial conditions are established. The Runge-Kutta method is used to integrate the differential equations for the following functions:

$$v_1 = R(t), \tag{3.1}$$

$$v_2 = \dot{R}(t), \tag{3.2}$$

$$v_3 = \left\langle (R/R_0)^4 \right\rangle, \tag{3.3}$$

$$v_4 = \left\langle (R/R_0)^{4-3\eta} \right\rangle. \tag{3.4}$$

The time averages in Eqs. (3.3) and (3.4) are defined by

$$\langle f \rangle = \frac{1}{T} \int_{t_0}^{t_0+T} f(t)\, dt,$$

where f is an arbitrary function.

Initially, the bubble has an equilibrium radius of $R(0) = R_{00}$, where R_{00} is the initial equilibrium radius. Throughout the thesis, the initial equilibrium radius is $R_{00} = 10\ \mu$m. The bubble wall velocity is initially at rest, and thus $\dot{R}(0) = 0$. The time averages $\langle (R/R_0)^4 \rangle$ and $\langle (R/R_0)^{4-3\eta} \rangle$ are initialized to zero. The respective differential equations for Eqs. (3.1)–(3.4) are

$$\dot{R} = S, \tag{3.5}$$

$$\dot{S} = \frac{1}{R\rho}\Bigg[\left(p_0 + \frac{2\sigma}{R_0}\right)\left(\frac{R_0}{R}\right)^{3\eta} - P_0 - \frac{2\sigma}{R} \tag{3.6}$$

$$- p_a(t) - \frac{4\mu}{R}\dot{R} - \rho R_0 \frac{\omega_0^2}{\omega}\left(b_r + b_t\right)\dot{R}\Bigg] - \frac{3\dot{R}^2}{2R},$$

$$\dot{f}_1 = \frac{1}{T}\left(\frac{R}{R_0}\right)^4, \tag{3.7}$$

$$\dot{f}_2 = \frac{1}{T}\left(\frac{R}{R_0}\right)^{4-3\eta}. \tag{3.8}$$

Equation (3.5) is the bubble wall velocity $\dot{R}(t)$. Equation (3.6) is the acceleration of the bubble wall $\ddot{R}(t)$ and is obtained by putting Eq. (2.12) in terms of $\ddot{R}$. Both Eqs. (3.5) and (3.6) correspond with Eq. (2.12). Equations (3.7) and (3.8) are the differential equations for Eqs. (3.3) and (3.4), respectively. To demonstrate this, Eq. (3.7) is integrated for one acoustic period:

$$f_1(t_0 + T) = f_1(t_0) + \frac{1}{T}\int_{t_0}^{t_0+T}\left(\frac{R}{R_0}\right)^4 dt, \tag{3.9}$$

where t_0 is the initial time for integration. If $f_1(t_0) = 0$, then Eq. (3.9) simplifies to

$$f_1(t_0 + T) = \frac{1}{T}\int_{t_0}^{t_0+T}\left(\frac{R}{R_0}\right)^4 dt = \left\langle (R/R_0)^4 \right\rangle, \tag{3.10}$$

and thus Eq. (3.10) is the time average of $(R/R_0)^4$. Identical analysis can be applied to Eq. (3.8) to produce Eq. (3.4). The time averages are reinitialized to zero after each acoustic cycle.

Before integrating Eq. (2.12), several parameters are assigned: drive frequency f, SPL, the initial time (t_{start}) and final time (t_{end}) for integration, number of integration/bubble excitation, steps per acoustic cycle, step size h, an error threshold for integration variables ϵ, and the polytropic index η. For this thesis, f is primarily in the range 100 Hz–10 kHz, but higher frequencies are also investigated. Sound pressure levels ranged from 205 dB–215 dB. The numerical integration algorithm implemented in this work was unable to integrate Eq. (2.12) for $p_a > 0.1$ MPa and $R_0 = 10$ μm (refer to Fig. 3.3). Typically, Eq. (2.12) is integrated for a time period of 10–20 acoustic cycles. The exact time period for integration is dependent upon the transient time for the driven bubble (refer to Fig. 3.1). The number of integration steps taken over an acoustic cycle was 500. The error threshold ϵ is calculated by taking the ratio of the truncation error to the maximum calculated change in the integration variable. For $\epsilon < 10^{-8}$, the present algorithm could successfully integrate Eq. (2.12) for $p_a \leq 0.1$ MPa.

The polytropic exponent η describes the heat exchange between the gas inside the bubble and its surrounding liquid.[13] The thermodynamic state of the bubble can potentially range from an isothermal state ($\eta = 1.0$) to an adiabatic state ($\eta = 1.4$), depending on the size of the bubble and the frequency of oscillation. When the bubble behaves isothermally, all heat gained or lost due to expansion or contraction is transferred to the heat reservoir of the surrounding liquid. No heat is exchanged between the bubble and the liquid in an adiabatic state.

The Runge-Kutta method is imbedded in a loop which stops execution when $t = t_{\text{end}}$. The following values are passed to the Runge-Kutta algorithm:

current values of Eqs. (3.1)–(3.4), the time t, step size h, an error threshold ϵ, and a minimum allowable step size $h_{\min}$. When the Runge-Kutta method is called, it attempts a step size h and calculates new values for Eqs. (3.1)–(3.4) based on Eqs. (3.5)–(3.8). If a step size h is completed without exceeding the error threshold ϵ, t is incremented by h, all parameters are updated, and the Runge-Kutta method is called again. If, after a step size h is attempted, the new values of Eqs. (3.1)–(3.4) exceed the error threshold ϵ, then a smaller step size is attempted until a succesful step is completed. Execution of the program stops when $h = 0$, which occured for $p_a > 0.1$ MPa and $R_{00} = 10\ \mu$m.

When the Runge-Kutta algorithm is first called ($t = 0$), the bubble is at rest. For $t > 0$, the bubble is insonified, causing the bubble wall to move. To satisfy the initial condition of $\dot{R} = 0$, the incident acoustic pressure is

$$p_{ac}(t) = p_a \sin \omega t, \tag{3.11}$$

where p_a is the acoustic pressure amplitude, and ω is the angular frequency of excitation.

To accurately model bubble growth using Eq. (2.10), Eqs. (3.3) and (3.4) are evaluated during periodic oscillation of the bubble radius, in which Eqs. (3.3) and (3.4) are constant. If the bubble oscillation is aperiodic, then the values of Eqs. (3.3) and (3.4) vary from cycle to cycle, which can lead to innacurate calculations for bubble growth when Eq. (2.10) is integrated. To estimate the duration of the transient state (time to reach periodic oscillation), the bubble is modelled as a linear, damped oscillator.[13] For small amplitudes of radial oscillation, the radius is $R = R_0 + x(t)$, where

$$\ddot{x} + \frac{\omega_0}{Q}\dot{x} + \omega_0^2 x = 0, \tag{3.12}$$

ω_0 is the Minnaert frequency of the bubble, and Q is the quality factor. The motion of the bubble is simple harmonic in this case. The quality factor Q can be related to the total dimensionless damping coefficient by $\delta_{\text{tot}} = 1/Q$,[13] which accounts for losses due to viscosity, acoustic radiation, and thermal damping. From linear theory, the transient part of the solution decays as $e^{\delta_{\text{tot}}\omega_0 t/2}$. The decay time $(1/e)$ is

$$\tau = \frac{2}{\delta_{\text{tot}}\omega_0}. \tag{3.13}$$

Values for δ_{tot} are taken from Fig. 3.20 of Leighton.[13] Figure 3.1(a) shows results for a 10 μm bubble driven at 10 kHz with SPL = 215 dB, where the decay time is approximately $\tau \approx 7\,\mu$s, and τ is approximately 10 percent of T. In Fig. 3.1(a), the transient period is not visible because the time period shown is 100 times larger than the transient state. In Fig. 3.1(b), R_0 is increased to 200 μm under the same excitation conditions. Equation (3.13) predicts that $\tau \approx 400\mu$s, which is 4 acoustic cycles. Thus, the transient state is more apparent in Fig. 3.1(b) than (a). After 12 acoustic cycles, the bubble radius is periodic.

To validate the model in Eq. (2.12), simulations are compared $R(t)$ with Fig. 4.7 of Ref. 13. The results in Fig. 3.2 are for a bubble with $R_0 =$ 0.1 mm, driven at f = 10 kHz, and p_a = 0.24 MPa. For $t <$ 0.65 ms, Figs. 3.2(a) and

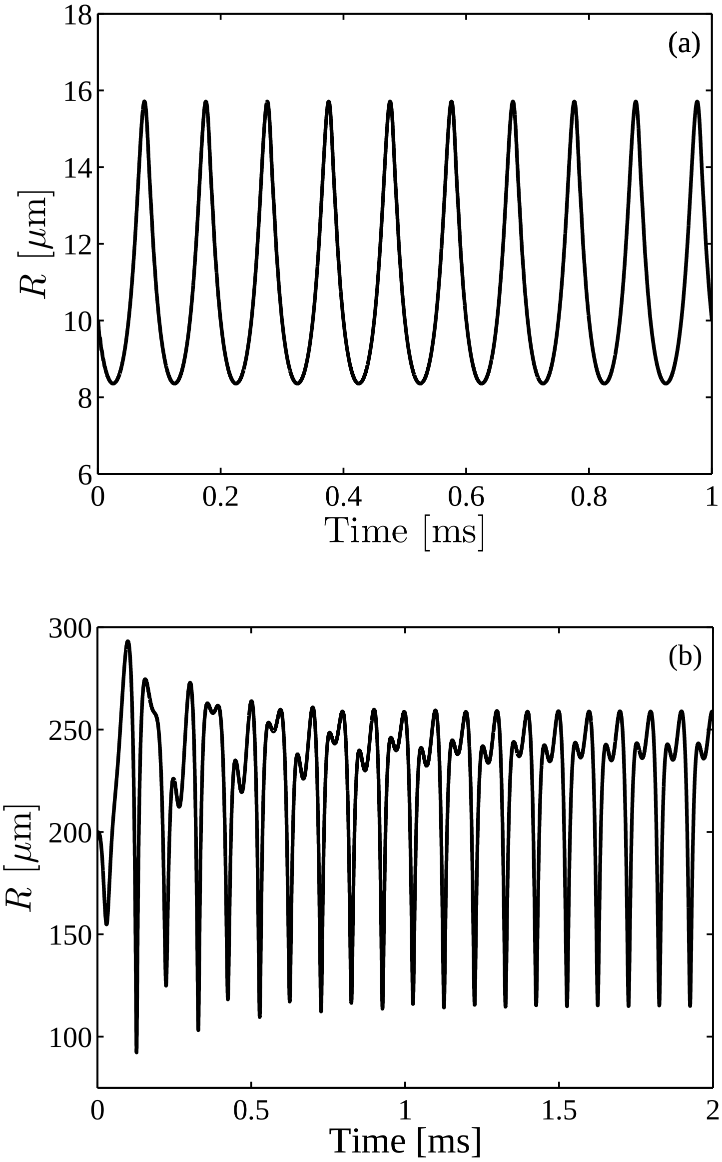

Figure 3.1: $R(t)$ for (a) $R_0 = 10\ \mu$m and (b) $R_0 = 200\ \mu$m, driven at $f = 10$ kHz and an SPL = 215 dB.

(b) are in close agreement. For $t \geq 0.65$ ms, the bubbles undergo different oscillations. Such discrepancies are not unexpected in numerical solutions following the abrupt changes associated with rebound. The close agreement up to 0.65 ms, even following several rebounds, is sufficient to establish the validity of the model for our purposes.

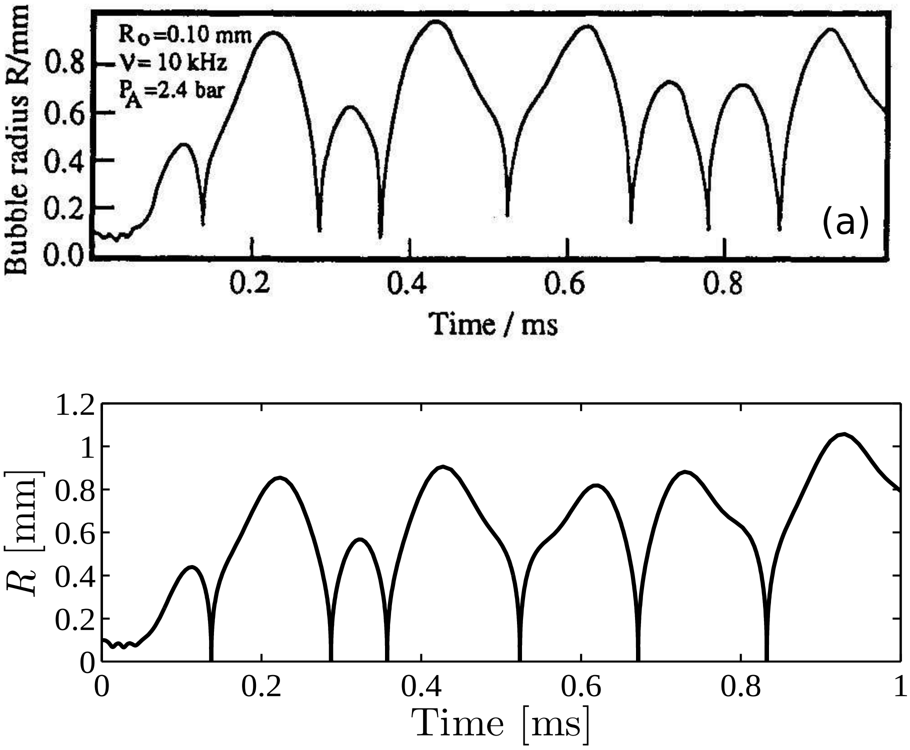

Figure 3.2: Comparison of $R(t)$ for a bubble driven at $f = 10$ kHz, $R_0 = 0.1$ mm, and $p_a = 0.24$ MPa. (a) is Fig. 4.7 of Leighton,[13] (b) $R(t)$ from simulations of Eq. (2.12).

The Runge-Kutta algorithm implemented here could not integrate Eq. (2.12) for SPL > 217 dB ($p_a > 0.1$ MPa), and bubble radius $R_0 = 10\ \mu$m. Figure

3.3(a) shows the time waveform of the acoustic pressure for $f = 10$ kHz and an amplitude of 0.24 MPa. In Fig. 3.3(b), a bubble with $R_0 = 10$ μm is driven at $f = 10$ kHz and $p_a = 0.24$ MPa. The frequency and pressure amplitude values were also utilized to generate Fig. 3.2. The key difference is that the bubble radius in Fig. 3.3(b) is 10 times smaller. The bubble in Fig. 3.2 is undergoing periodic oscillations, while the bubble in Fig. 3.3(b) undergoes a violent collapse when the acoustic pressure becomes compressional. Smaller bubbles have higher resonance frequencies, which cause them to react on smaller time intervals.[13] When the acoustic pressure starts to compress the bubble, the potential energy stored in the gas during the expansion phase causes the bubble to collapse violently. In Fig. 3.3(c), the pressure amplitude is reduced to $P_a = 0.14$ MPa (SPL = 220 dB). The bubble still collapses when the acoustic wave becomes compressional. Acoustic pressure amplitudes of this magnitude are of interest because they are the largest pressure amplitudes used by Crum and Mao.[12]

3.2 Numerical Integration of Fyrillas-Szeri Equation

Equation (2.10) is numerically integrated using the same fourth-order, adaptive step size Runge-Kutta algorithm as used for the integration of Eq. (2.12). Integration of Eq. (2.10) results in an updated equilibrium radius R_0 after a time interval Δt, which is 10–20 acoustic cycles depending on the frequency. There are three time averages in Eq. (2.10) in which two, Eqs. (3.3) and (3.4),

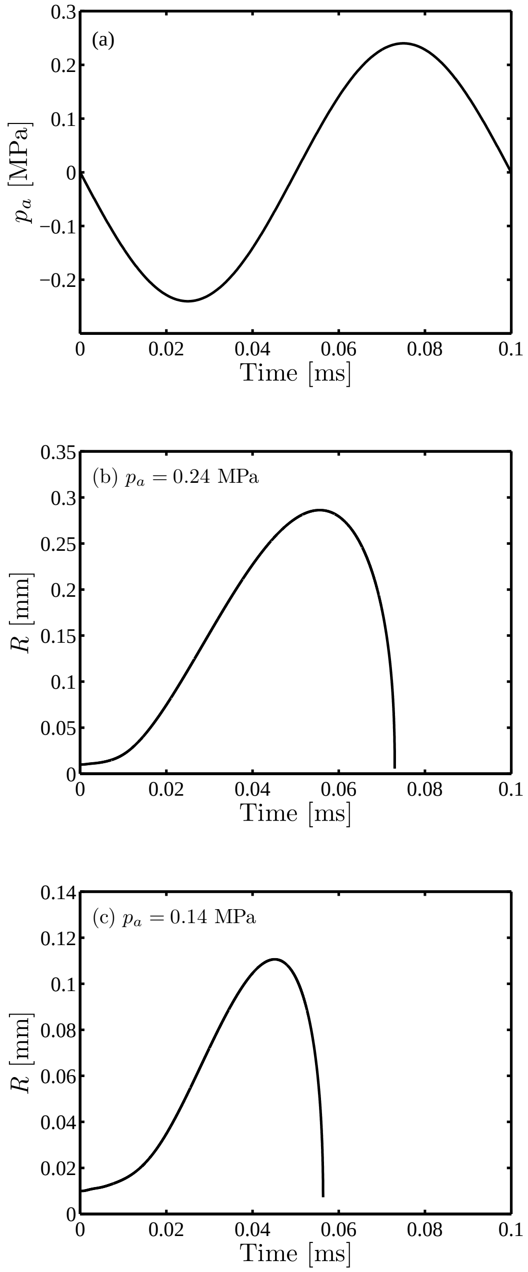

Figure 3.3: $R(t)$ for bubbles driven at $f = 10$ kHz and $R_0 = 10$ μm. The acoustic pressure function is shown in (a). $R(t)$ with $p_a = 0.24$ MPa is shown in (b), and $R(t)$ with $p_a =$ 0.14 MPa is shown in (c).

are calculated during integration of Eq. (2.12). The third time average,

$$I = \int_0^\infty \frac{dx}{\left\langle \left[3x + (R/R_0)^3\right]^{\frac{4}{3}} \right\rangle}, \tag{3.14}$$

is evaluated before integration of Eq. (2.10). Some analysis is required to appropriately determine the upper limit of integration, since numerical integration to infinity is not possible. First, the integral is evaluated over two intervals:[21]

$$I_1 = \int_0^{x_0} \frac{dx}{\langle [3x + (R/R_0)^3]^{4/3} \rangle}, \tag{3.15}$$

$$I_2 = \int_{x_0}^\infty \frac{dx}{\langle [3x + (R/R_0)^3]^{4/3} \rangle}, \tag{3.16}$$

such that $I = I_1 + I_2$. The change of variable

$$u = x^{-1/3}, \tag{3.17}$$

$$du = -\frac{1}{3} x^{-4/3} dx, \tag{3.18}$$

is used to obtain

$$I_2 = 3^{-1/3} \int_0^{x_0^{-1/3}} \frac{du}{\langle [1 + [u^3 (R/R_0)^3]/3]^{4/3} \rangle}. \tag{3.19}$$

The integral can be evaluated over a finite interval. The value of x_0 is arbitrary and we chose $x_0 = 1$.

After Eqs. (3.3), (3.4), and (3.14) are evaluated, R_0 is calculated after a time interval Δt using Eq. (2.10), which is integrated using the Runge-Kutta method used for integration of Eq. (2.12). To integrate Eq. (2.10), values are assigned for t_{start}, t_{end}, the time step h, the minimum time step

$h_{\min}$, the number of integration steps, and an error tolerance ϵ. Although rectified diffusion is a slow process[13] and previous research calculated bubble growth rates in microns per minute,[17,28] R_0 is calculated after every 0.02 s (f = 100 Hz) to 0.0002 s (f = 10 kHz), depending on the frequency. For this range of time steps, h was successful for $\epsilon \leq 0.05$. The error threshold was never exceeded during integration of Eq. (2.10), and thus Eq. (2.10) was integrated without the Runge-Kutta method stopping code execution.

The equilibrium radius R_0 is typically calculated from $t = 0$–100. First, Eq. (2.12) is integrated from $t = 0$, to $t = \Delta t$ to evaluate Eqs. (3.3) and (3.4). Then, Eq. (2.10) is integrated from $t = 0$ to $t = \Delta t$ to calculate the growth or decrease in R_0 over this same time period. The updated value of R_0 is then used by Eq. (2.12), and Eq. (2.12) is integrated for an additional Δt. The updated values of Eqs. (3.3) and (3.4) are used by Eq. (2.10) to calculate the current R_0. This process continues until $t = 100$.

3.2.1 Verification of Our Implementation of the Fyrillas-Szeri Equation

To confirm that the algorithm for evaluation of Eq. (2.10) is accurate, results are compared with data from Crum and Mao[12] and Ilinskii et al.[18] The Ilinskii model is considered to be the more accurate of the two models primarily because it does not assume a large Péclet number. Other details of this algorithm are discussed in Chapter 1. Figure 3.4 compares $R_0(t)$ from Crum and Mao[12] [Fig. 3.4(a)] with our data [Fig. 3.4(b)] for f = 500 Hz,

$R_{00} = 10\,\mu$m, and a gas supersaturation of 200% . In this thesis, we will refer to gas saturations in terms of percents and the equivalent ratio C_i/C_0. Due to Henry's Law, the concentration of a gas in solution is proportional to the partial pressure of that gas acting on the liquid-gas interface.

In Fig. 3.4(a), the bubble is exposed to SPL ranging from 150 dB–220 dB. There is negligible bubble growth for SPL between 150 dB and 200 dB for $C_i/C_0 = 2.0$, implying that static diffusion is the dominant growth mechanism. Evaluations of Eqs. (3.3), (3.4), and (3.14) will be invariant for these SPL. When the SPL is increased to 210 dB, there is noticable growth in the final R_0 of approximately 2.5 μm. Figure 3.4(a) contains two curves for an SPL = 220 dB. The lower curve is data generated by the Eller-Flynn equation,[15] and the upper curve corresponds with Eq. (2.10).[17] The Fyrillas-Szeri equation implements a more rigorous approach to rectified diffusion than the Eller-Flynn equation because it is not limited to infinitesimal bubble oscillations and rectified diffusion thresholds.[12,17] Figure 3.4(b) has data for SPL ranging from 190 dB–215 dB. Data shown in Figs. 3.4(a) and (b) are in very close agreement for SPL up to 200 dB. Figure 3.4(b) does not contain data for an SPL = 220 dB for reasons described earlier in this section (refer to Fig. 3.3).

Figures 3.5(a)–(d) compare $R_0(t)$ for our implementation of Eq. (2.10) and the Ilinskii model.[18] In Fig. 3.5, $R_{00} = 10$ μm, $f = 100$ Hz, $C_i/C_0 = 1.5$, and the exposure level varies from static diffusion to SPL = 215 dB. The only significant difference in the models occurs for 215 dB. The final equilibrium radius values for the Ilinskii model and Eq. (2.10) are 110 μm and 104 μm,

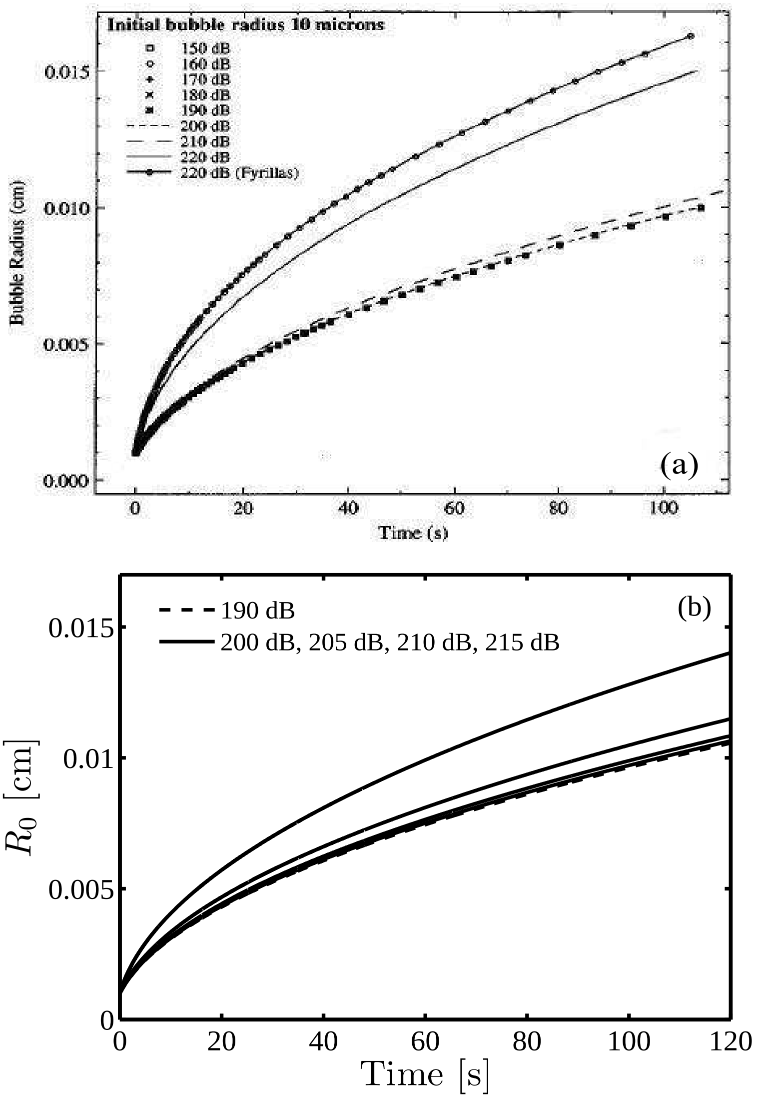

Figure 3.4: Plots comparing $R_0(t)$ for f = 500 Hz, and C_i/C_0 = 2.0. Plot (a) is reproduced from Crum and Mao[12] and contains data from Fyrillas and Szeri,[17] and (b) contains data from our implementation of Eq. (2.10). Plot (a) contains two curves for SPL = 220 dB, with each curve corresponding to a different model for rectified diffusion. The top curve for SPL = 220 dB was generated by Eq. (2.10) and the bottom curve was generated by the Eller-Flynn equation.[15] Plot (b) does not contain data for an SPL = 220 dB. In (b), the solid lines are in increasing SPL from bottom to top. Thus, the bottom solid line is for an SPL = 190 dB, and the top line is for SPL = 215 dB.

respectively, leading to decrease in bubble size of approximately 6%. This percent decrease is within the 10%–20% stated by Ilinskii et al. to occur in other models al.[18]

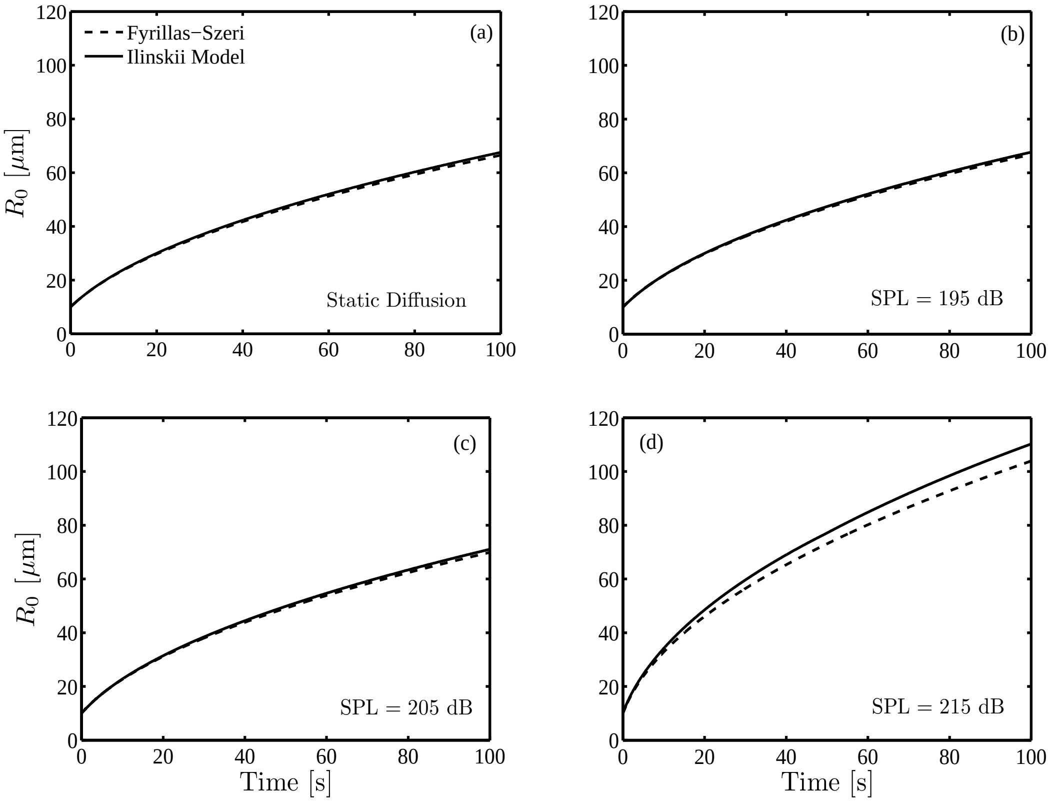

Figure 3.5: Comparison of $R_0(t)$ between Eq. (2.10)[17] and the Ilinskii et al. model[18] for f = 100 Hz, C_i/C_0 = 1.5, and various SPLs. Plot (a) contains data for static diffusion, (b) SPL = 195 dB, (c) SPL = 205 dB, and (d) SPL = 215 dB.

In Figs. 3.6(a)–(d), C_i/C_0 is increased to 3.0. Ilinskii et al.[18] predict that there will be a greater difference in R_0 when the supersaturation is increased. When supersaturation is high (250%–300%), previous models of rectified diffusion underestimate the influx of gas into a bubble. When the supersaturation level is high, initial bubble growth occurs primarily because of static diffusion which yields a Péclet number that is not large. The noticable difference again occurs for an SPL = 215 dB. In Fig. 3.6, there is a noticable difference in R_0 for all exposure levels. The greatest underestimation of R_0 occurs in Fig. 3.6(d) when the SPL = 215 dB. For this case, the final equilibrium radius calculated by Eq. (2.10) is approximately 10% smaller than the final equilibrium radius calculated by the Ilinskii model. Since data from our implementation of Eq. (2.10) agrees well with a previous implementation,[12] and is within the error range predicted by the Ilinskii model,[18] we conclude that our implementation of Eq. (2.10) will provide sufficient accuracy for our parameter range.

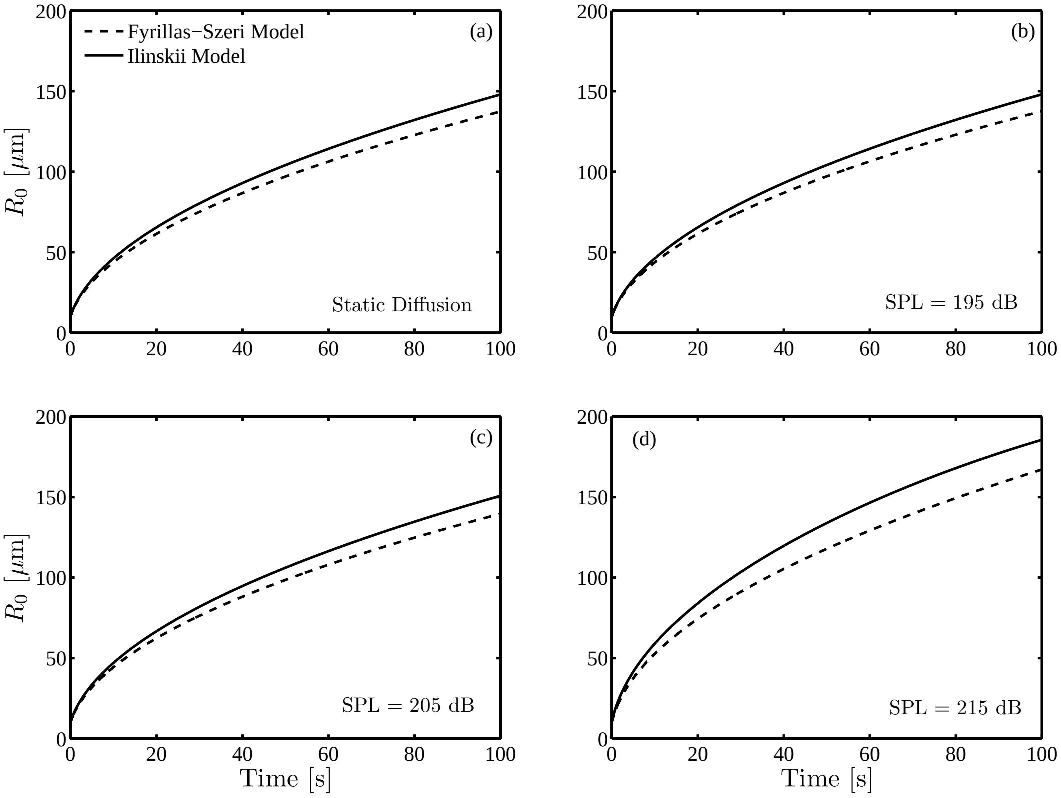

Figure 3.6: Comparison of $R_0(t)$ between Eq. (2.10)[17] and the Ilinskii et al. model[18] for f = 100 Hz, C_i/C_0 = 3.0, and various SPLs. Plot (a) contains data for static diffusion, (b) SPL = 195 dB, (c) SPL = 205 dB, and (d) SPL = 215 dB.

Chapter 4

Results

In this chapter, numerical simulations are presented for bubble growth due to rectified diffusion and static diffusion. The bubble is enclosed by incompressible, nitrogen supersaturated water at 20 °C. The concentration gradient between the gas in the bubble and the dissolved gas in the fluid enables the transfer of gas between the bubble and the liquid. In the model to be discussed, the bubble wall does not impede gas transfer with the fluid. The bubble's growth is unbounded. Surface tension acts on the bubble, which increases the pressure inside the bubble over the pressure outside the bubble. But, the bubble will not dissolve due to the supersaturated water surrounding the bubble. For a bubble with $R_0 = 10\ \mu$m, a supersaturation of 113.5% prevents dissolution.[12]

Results are presented for several cases of rectified diffusion and static diffusion. First, bubble growth is considered during continuous insonification for a range of monofrequency signals, gas supersaturations, and SPLs. How the instantaneous bubble radius $R(t)$ influences bubble growth is investigated. Second, bubble growth data due to continuous insonification are compared with bubble growth data due to model sonar signals, including monofrequency sonar signals and an HFM sweep. The chapter concludes with simulations of bubble growth for conditions potentially present in surfaced marine mammals for both rectified diffusion and static diffusion.

4.1 Bubble Growth due to a Continuous Wave Source

The first set of results pertains to a bubble which is continuously insonified by a monofrequency acoustic source. Driving frequencies f range from 100 Hz to 100 kHz. Sound pressure levels vary from 205 dB to 215 dB re 1 μPa. The initial equilibrium bubble radius is $R_{00} = 10$ μm, which was selected because it is of sufficient size to pass through the lungs but still can potentially cause tissue displacement and embolism.[14] The values used for C_i/C_0 are 1.5, 2.0, and 3.0. The ratio C_i/C_0 represents the ratio of the concentration of gas far from the bubble (C_i) to the gas concentration adjacent to the bubble wall under atmospheric pressire (C_0). The term C_0 does not account for the additional gas concentration in the liquid adjacent to the bubble wall (C_R) due to the additional pressure exerted on the bubble from surface tension. Gas concentration is measured in moles per unit volume. Parameter values used in this thesis, which are based on those used by Crum and Mao,[12] are presented in Table 4.1. Before discussing change in the equilibrium radius R_0, the influence of the instantaneous bubble radius R on bubble growth is discussed.

4.1.1 Instantaneous bubble radius

Integration of Eq. (2.10) requires evaluation of the time averages in Eqs. (3.3), (3.4), and (3.14). The time averages are calculated from data generated by the numerical integration of Eq. (2.12). In Fig. 4.1(a), $R_0(t)$ is shown for a bubble with $R_{00} = 10\ \mu$m, $f = 10$ kHz, and $C_i/C_0 = 3.0$. Bubble growth is calculated for static diffusion (i.e., no acoustic pressure) and for SPL = 205 dB, 210 dB, and 215 dB. The curves are stacked by increased sound pressure level. In Figs. 4.1(b)–(j), the instantaneous bubble radius R is shown for one acoustic cycle. Figures 4.1(b)–(d) show $R(t)$ at SPL = 205 dB for 0 s, 50 s, and 99 s respectively. Figures 4.1(e)–(g) follow the same format for SPL = 210 dB, and Figs. 4.1(h)–(j) for SPL = 215 dB. For $R_{00} = 10\ \mu$m and $f = 100$ Hz–10 kHz, bubble growth is negligible relative to static diffusion for SPL < 205 dB.

During static diffusion, the bubble is not driven acoustically, and the time averages (which are calculated over one acoustic cycle) in Eqs. (3.3), (3.4),

water density:	$\rho = 1000$ kg/m^3
surface tension:	$\sigma = 0.072$ N/m
atmospheric pressure:	$p_0 = 101$ kPa
shear viscosity:	$\mu = 0.001$ Pa $\cdot$ s
diffusivity constant:	$D = 2.4 \times 10^{-9}$ m^2/s
constant:	$d = kTC_0/p_0 = 2.0 \times 10^{-2}$
universal gas constant:	$k = 8.314$ J/mol $\cdot$ K
water temperature:	$T = 20°$C

Table 4.1: Parameter values, which are based used by simulations in this thesis.[12]

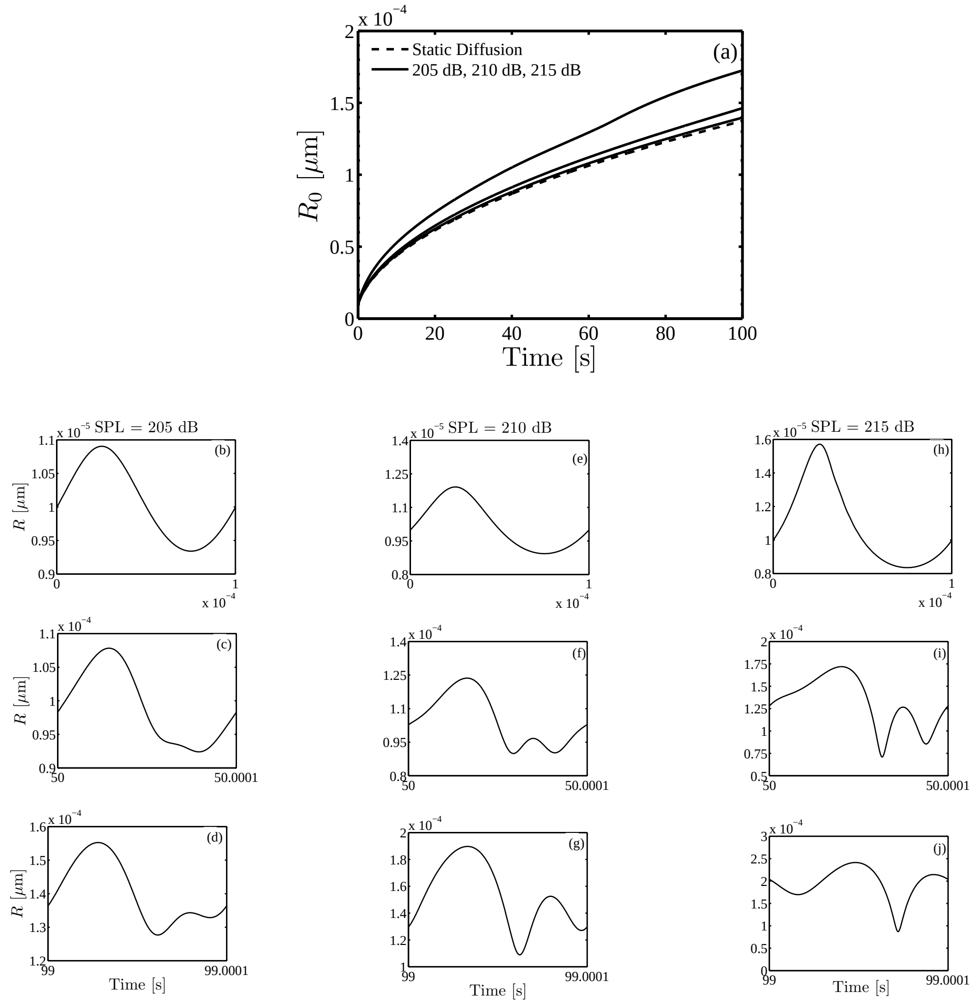

Figure 4.1: Equilibrium radius versus time and instantaneous radius versus time for $R_{00} = 10\ \mu$m, $f = 10$ kHz, and $C_i/C_0 = 3.0$. Plot (a) contains $R_0(t)$ data for static diffusion, and SPL = 205 dB, 210 dB, and 215 dB . The curves in (a) are arranged by increasing SPL. Plots (b)–(d), (e)–(g), and (h)–(j) show $R(t)$ at different times on the $R_0(t)$ curve for SPL = 205 dB, 210 dB, and 215 dB.

and (3.14) are equal to one. Therefore, $R(t) = R_0(t)$, and Eq. (2.10) becomes

$$\frac{dR_0}{dt} = \frac{Dd}{R_0}\left(1 + \frac{4\sigma}{3R_0 p_0}\right)^{-1}\left[\frac{C_i}{C_0} - \left(1 + \frac{2\sigma}{R_0 p_0}\right)\right]. \tag{4.1}$$

The change in equilibrium radius can be estimated numerically. Using the data in Fig. 4.1, at $t = 0$, $dR_0/dt \approx 8$ μm/s. When the bubble radius is ten times larger ($R_0 = 100$ μm), the growth rate is 0.9 μm/s. Thus, the growth rate of the bubble for static diffusion is approximately inversely proportional to R_0, or

$$\frac{dR_0}{dt} = \frac{B}{R_0}, \tag{4.2}$$

where B is a constant that can be estimated from Eq. (4.1). The term $4\sigma/3R_0 p_0$ is initially equal to 0.095, but is inversely related to R_0. As the bubble grows, $4\sigma/3R_0 p_0 \to 0$, which leads to $(1 + 4\sigma/3R_0 p_0) \to 1$. Similarly, the term $(1 + 2\sigma/R_0 p_0) \to 1$ as R_0 increases. After significant bubble growth during static diffusion, Eq. (4.1) can be approximated by

$$\frac{dR_0}{dt} = \frac{Dd}{R_0}\left(\frac{C_i}{C_0} - 1\right), \tag{4.3}$$

which leads to $B = Dd(C_i/C_0 - 1)$. Solving Eq. (4.3) yields

$$R_0 = R_{00}\left(1 + \frac{2CDd}{R_{00}^2}t\right)^{1/2}. \tag{4.4}$$

For $C_i/C_0 = 3.0$, we set $B = 1.98Dd$ and present the results in Fig. 4.2. The factor of 1.98 is close to the value of $C_i/C_0 - 1.0$, but the factor is not 2.0 due to the time it takes for $(1 + 4\sigma/3R_0 p_0) \to 1$ and $(1 + 2\sigma/R_0 p_0) \to 1$.

For rectified diffusion, Eq. (2.10) depends on the bubble's response R/R_0, and thus Eqs. (3.3), (3.4), and (3.14) do not have the value of one. As

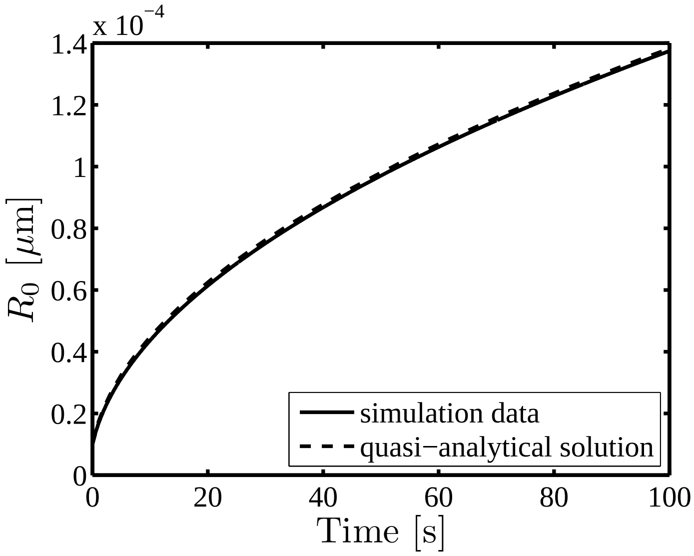

Figure 4.2: Simulation data of $R_0(t)$ plotted with Eq. 4.4 for $C = 1.98$, $R_{00} = 10\ \mu$m, and $C_i/C_0 = 3.0$.

SPL increases, the ratio R/R_0 increases, and therefore Eqs. (3.3) and (3.4) will increase as well. For example, at $t = 0$ and for SPL = 215 dB, the ratio of the maximum bubble radius to the minimum bubble radius is 1.9. After 99 s, the ratio increases to 3.1. Figure 4.3 shows Eqs. (3.3), (3.4), and (3.14) and the ratio of (3.4) to (3.3) in Figs. 4.3(a)–(d), respectively. The parameter values are $R_{00} = 10\ \mu$m, $f = 10$ kHz, SPL = 215 dB, and $C_i/C_0 = 3.0$. The peak in Figs. 4.3(a)–(c) at $t = 30$ s indicate that the bubble is being driven at resonance. During stable cavitation, and analogous to linear oscillators, the bubble's response is greatest when excited at resonance. Hence, Eqs. (3.3) and (3.4), and the inverse of Eq. (3.14) will be greatest during resonance. Figure 4.4 is similar to Fig. 4.3 except that $f = 1$ kHz. During the time interval shown, the bubble is not driven at resonance. After 10 s, the rate of bubble growth decreases, which can be seen in Figs. 4.4(c) and (d). When the equilibrium radius R_0 is 10 times its original size, the ratio of Eq. (3.4) to Eq. (3.3) is approximately the only quantity subtracted from C_i/C_0. Thus, bubble growth is greatest when the ratio is least.

For parameter values used in this thesis and for SPL < 205 dB, the time average of $R/R_0 \approx 1$, which causes Eqs. (3.3), (3.4), and (3.14) to be unity. If the ratio of Eq. (3.4) to Eq. (3.3) is unity and the inverse of Eq. (3.14) is unity as well, then the equation for rectified diffusion, Eq. (2.10), becomes the equation for static diffusion, Eq. (4.1). Thus, for the parameter values used in this thesis, significant bubble growth due to rectified diffusion did not occur for SPL < 205 dB.

4.1.2 Analysis of Bubble Growth for Continuous Insonification

In this section, bubble growth during rectified diffusion is investigated by varying SPL, nitrogen gas supersaturation ratio C_i/C_0, and driving frequency f. Figure 4.5 shows $R_0(t)$ for $f = 1$ kHz at (a) $C_i/C_0 = 1.5$ and (b) $C_i/C_0 = 3.0$. Similar to Fig. 4.1, bubble growth increases as the SPL is increased. Table 4.2 summarizes the data in Fig. 4.5. For SPL = 215 dB and $C_i/C_0 = 1.5$, the final equilibrium radius $R_0(t_f)$, where $t_f = 100$ s, is less than a bubble undergoing static diffusion for $C_i/C_0 = 3.0$. For both gas supersaturation ratios, there is a significant increase in the equilibrium radius as the SPL is increased from 210 dB to 215 dB. Of interesting note, the increase in

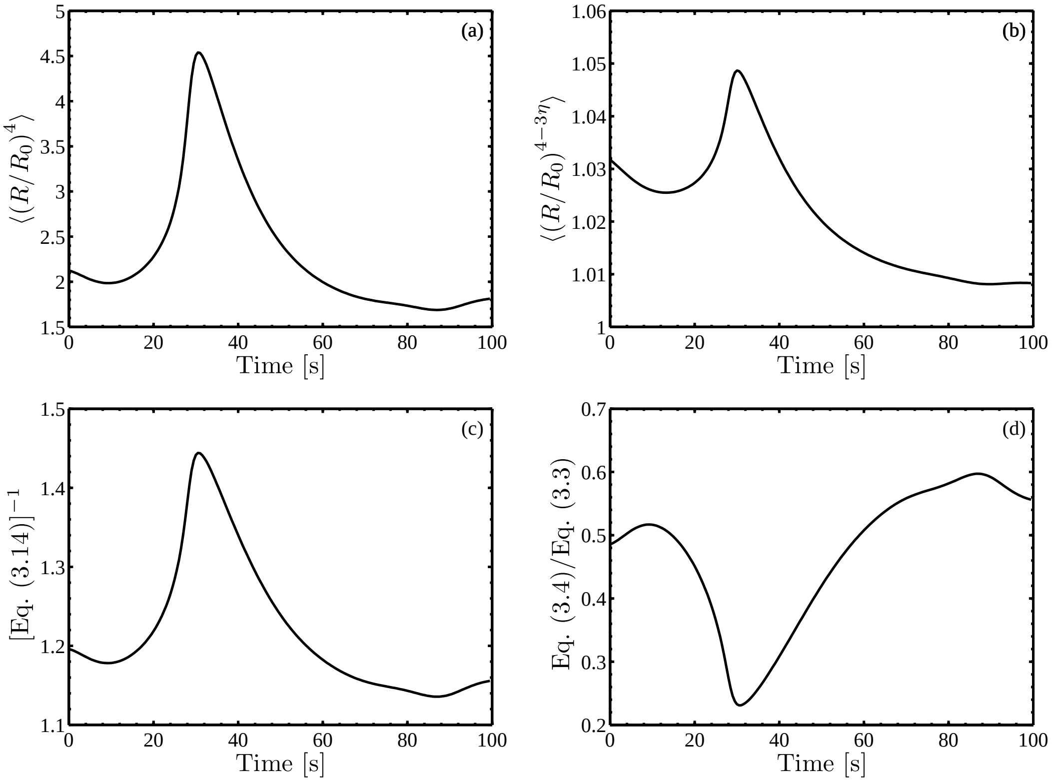

Figure 4.3: Plot (a) shows $\langle (R/R_0)^4 \rangle$ for a bubble with $R_{00} = 10\ \mu$m, $f = 10$ kHz, SPL = 215 dB, and $C_i/C_0 = 3.0$. Plot (b) shows $\langle (R/R_0)^{4-3\eta} \rangle$, plot (c) is the inverse of Eq. (3.14), and (d) is the ratio of Eq. (3.4) to Eq. (3.3). Resonance occurs at $t = 30$ s

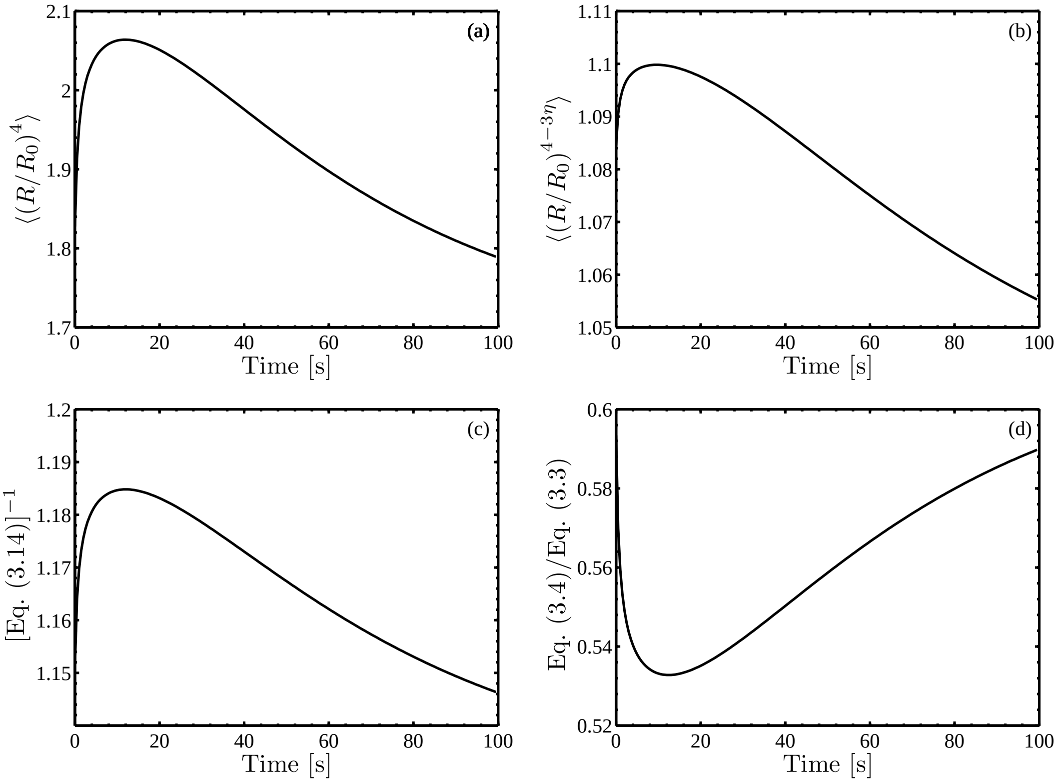

Figure 4.4: Plot (a) shows $\langle (R/R_0)^4 \rangle$ for a bubble with $R_{00} = 10$ μm, $f = 1$ kHz, SPL = 215 dB, and $C_i/C_0 = 3.0$. Plot (b) shows $\langle (R/R_0)^{4-3\eta} \rangle$, plot (c) is the inverse of Eq. (3.14), and (d) is the ratio of Eq. (3.4) to Eq. (3.3).

$R_0(t_f)$ from $C_i/C_0 = 1.5$ to $C_i/C_0 = 3.0$ is almost constant for each exposure level presented. Hence, increasing the gas supersaturation increases R_0 by a constant amount regardless of the SPL.

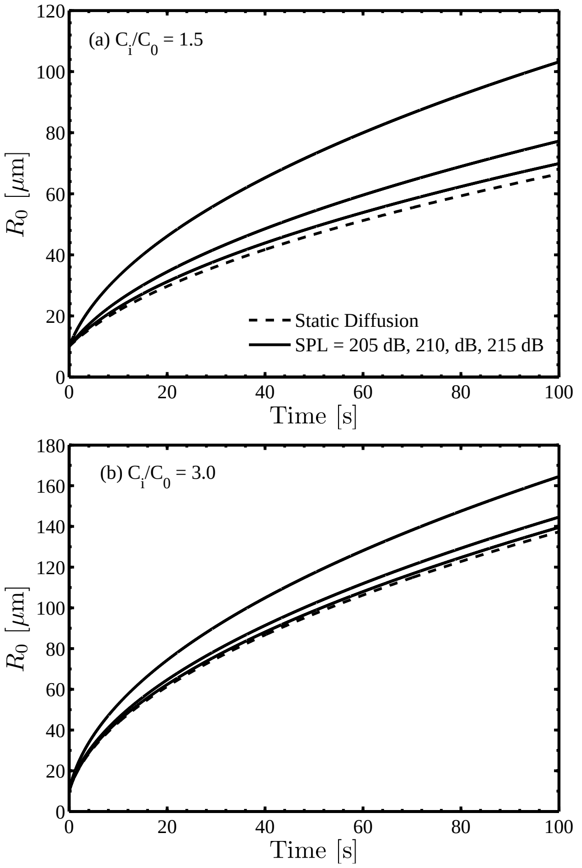

Figure 4.5: Equilibrium radius versus time for $R_{00} = 10$ μm and $f = 1$ kHz. The bubble is exposed to SPL = 205 dB, 210 dB, and 215 dB. Plot (a) shows $R_0(t)$ for $C_i/C_0 = 1.5$, and (b) shows $R_0(t)$ for $C_i/C_0 = 3.0$. Bubble growth increases with increasing SPL.

When analyzing the ratio of $R_0(t)$ at a given SPL to $R_0(t)$ during static diffusion, the percent increase in bubble radius is almost constant after 10 s.

Figure 4.6(a) shows the percent increase in $R_0(t)$ for SPL = 205 dB, 210 dB, and 215 dB relative to static diffusion at $C_i/C_0 = 1.5$. Therefore, the equilibrium radius of a bubble growing by rectified diffusion is proportional to the equilibrium radius of a bubble growing via static diffusion. For example, if $R_0(t)$ is calculated for static diffusion at $C_i/C_0 = 1.5$, then $R_0(t)$ for SPL = 215 dB can be calculated after 10 s by

$$R_0(t) = 1.55 \times R_0(t)_{\text{stat}}, \text{ for } t > 10\,\text{s}, \tag{4.5}$$

where the constant factor of 1.55 was obtained from the percent increase in bubble radius relative to static diffusion. In Fig. 4.6(b), a similar relationship is shown for $C_i/C_0 = 3.0$. The percent increase in R_0 relative to static diffusion is less for $C_i/C_0 = 3.0$. As can be seen in Fig. 4.6(b), the percent increase in R_0 is not constant for SPL = 215 dB. As time progresses, $\dot{R}_0$ for SPL = 215 dB decreases relative to $\dot{R}_0$ for static diffusion. The results shown in Fig. 4.6 do not apply for a bubble that passes through resonance (refer to Fig. 4.7 for $f = 100$ kHz).

In Fig. 4.7, how the driving frequency f affects $R_0(t)$ is investigated. From left to right, the columns show $R_0(t)$ for $C_i/C_0 = 1.5$ and 3.0. The

SPL (dB)	$R_0(t_f)$ (μm) for $C_i/C_0 = 1.50$	$R_0(t_f)$ (μm) for $C_i/C_0 = 3.0$
0	65.5	137
205	69.9	140
210	77.2	145
215	103	164

Table 4.2: $R_0(t_f)$ for $R_{00} = 10$ μm and $f = 1$ kHz.

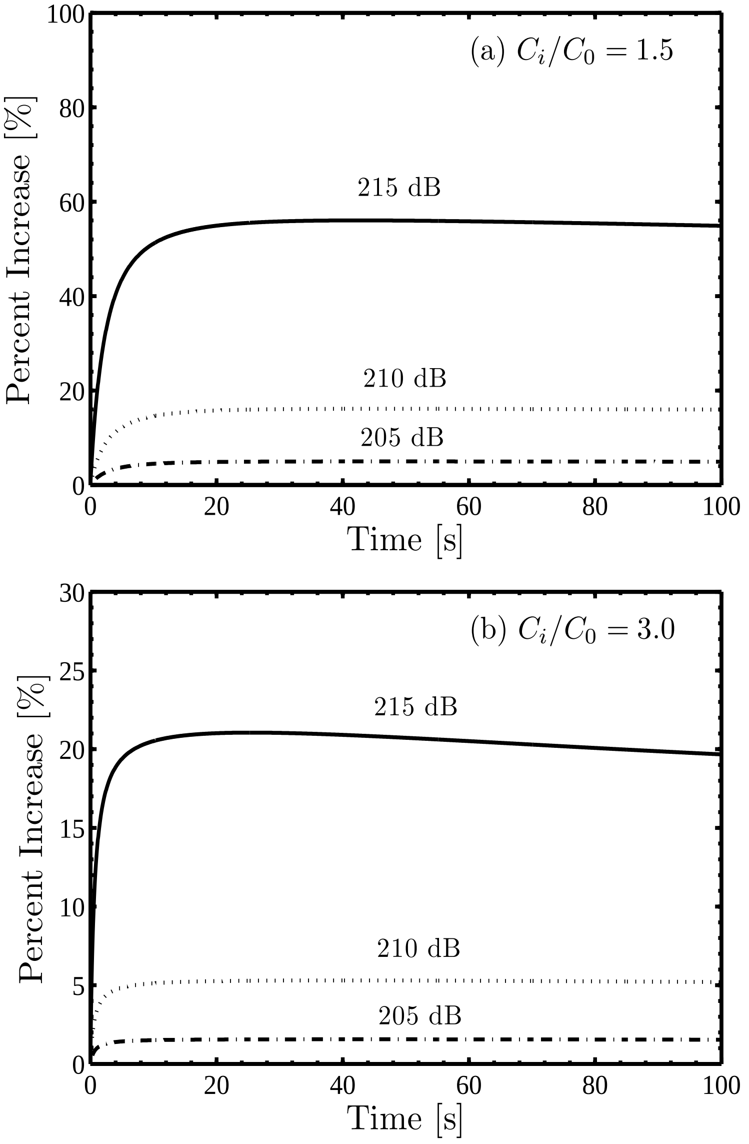

Figure 4.6: Percent increase in R_0 relative to static diffusion for $R_{00} = 10$ μm and $f = 1$ kHz. Plot (a) shows the percent increase in R_0 for $C_i/C_0 = 1.5$ and (b) shows the percent increase in R_0 for $C_i/C_0 = 3.0$.

rows in Fig. 4.7 contain $R_0(t)$ for driving frequencies of 100 Hz, 10 kHz, and 100 kHz. The bubble is excited by SPL = 205 dB, 210 dB, and 215 dB, and $R_0(t)$ is also shown for static diffusion. When $C_i/C_0 = 1.5$, there is virtually no difference in the $R_0(t)$ curves as the driving frequency is increased from 100 Hz to 10 kHz [Figs. 4.7(a) and (c)]. The bubble is driven far below resonance in Figs. 4.7(a) and (c), causing the bubble's response to be frequency independent. In Fig. 4.7(e), the driving frequency is $f = 100$ kHz and the bubble is driven at resonance when $R_0 = 30$ μm. It is evident in Figs. 4.7(e) and (f) when the bubble is being driven at resonance by looking at the sharp increase in the equilibrium radius when $R_0 = 30$ μm. After the bubble passes through resonance, the growth rate of the equilibrium radius decreases significantly and is approximately equal to the growth rate during static diffusion. Equal growth rates in Figs. 4.7(e) and (f) can be seen visually after the bubble passes resonance by observing that the curves are roughly parallel after resonance.

When the gas supersaturation is increased to 300%, there is virtually no difference between a bubble driven at $f = 100$ Hz, Fig. 4.7(b), and at 10 kHz, Fig. 4.7(d), until SPL = 215 dB. After 100 s of insonification, the increase in R_0 for $f = 10$ kHz is 5.4 μm, or 3% larger than $R_0(t_f)$ for $f = 100$ Hz. The increase in R_0 occurs because a bubble being driven at 10 kHz is closer to resonance than a bubble being driven at $f = 100$ Hz. At $t = 100$ s, we find $f_0/f \approx 1.8$ for $f = 10$ kHz, but $f_0/f \approx 170$ for $f = 100$ Hz. The resonance frequency is calculated using Eq. (2.14). A bubble being driven at 10 kHz will have a greater response to the forcing function, which increases the time average of R/R_0, which in turn increases the bubble's growth. In Fig. 4.7(f), the bubble passes through resonance after $t = 10$ s and its growth is driven by static diffusion thereafter.

Figure 4.8 shows the equilibrium radius for $C_i/C_0 = 1.5$, 2.0, and 3.0; f ranging from 100 Hz to 10 kHz; and SPL = 190 dB, 205 dB, 210 dB, and 215 dB. When the sound pressure level is 190 dB, there is no variation in $R_0(t_f)$ across the parameter range. For $R_{00} = 10$ μm and the parameter range chosen, the level SPL = 190 dB will not cause more bubble growth than static diffusion. In Figs. 4.8(a) and (b) ($C_i/C_0 = 1.5$ and 2.0, respectively), the final equilibrium radius is frequency invariant for the SPL shown. In Fig. 4.8(c), where $C_i/C_0 = 3.0$, there is an increase in R_0 as the frequency increases to 10 kHz. As explained in the previous paragraph, the bubble driven at 10 kHz is closer to resonance than at the lower driving frequencies. As the bubble approaches resonance, the response for the bubble increases and the time averages of R/R_0 increase, which leads to an increase in bubble growth.

For a bubble undergoing adiabatic oscillations without surface tension, a simple model for the resonance frequeny of the bubble is

$$f_0 = \frac{1}{2\pi R_0}\sqrt{\frac{3\gamma p_0}{\rho}}. \tag{4.6}$$

The resonance frequency, originally given by Minnaert,[30] is inversely proportional to R_0. For real bubbles, γ must be replaced by η, the polytropic index, which is not constant and gradually increases from 1.0 to 1.4 as R_0 in-

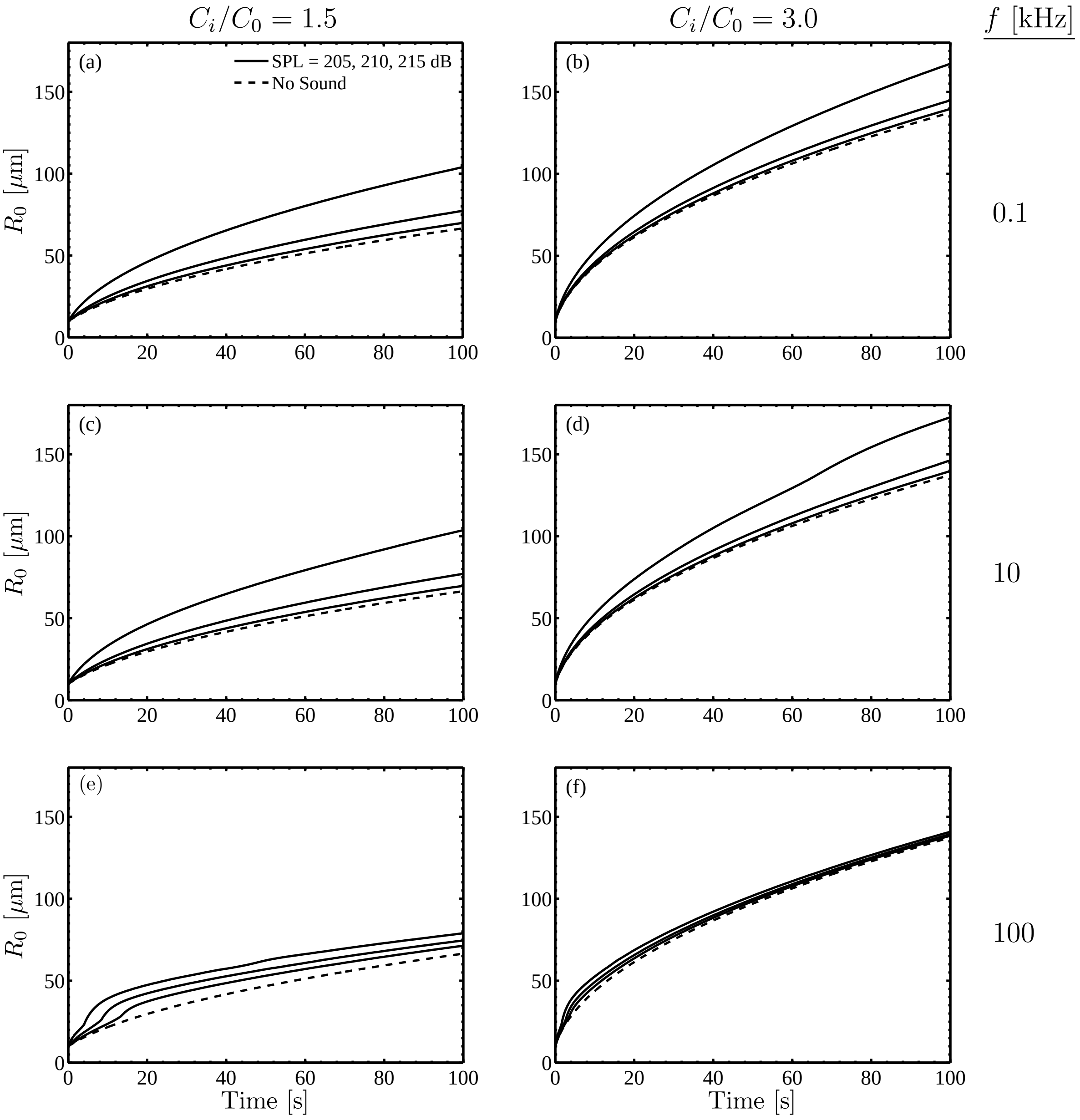

Figure 4.7: Equilibrium radius for a range of frequencies and gas supersaturations. In increasing order, the rows contain data for $f = 100$ Hz, 10 kHz, and 100 kHz. From left to right, the columns contain $R_0(t)$ for $C_i/C_0 = 1.5$ and 3.0. Each plot contains data for static diffusion and SPL = 205 dB, 210 dB, and 215 dB.

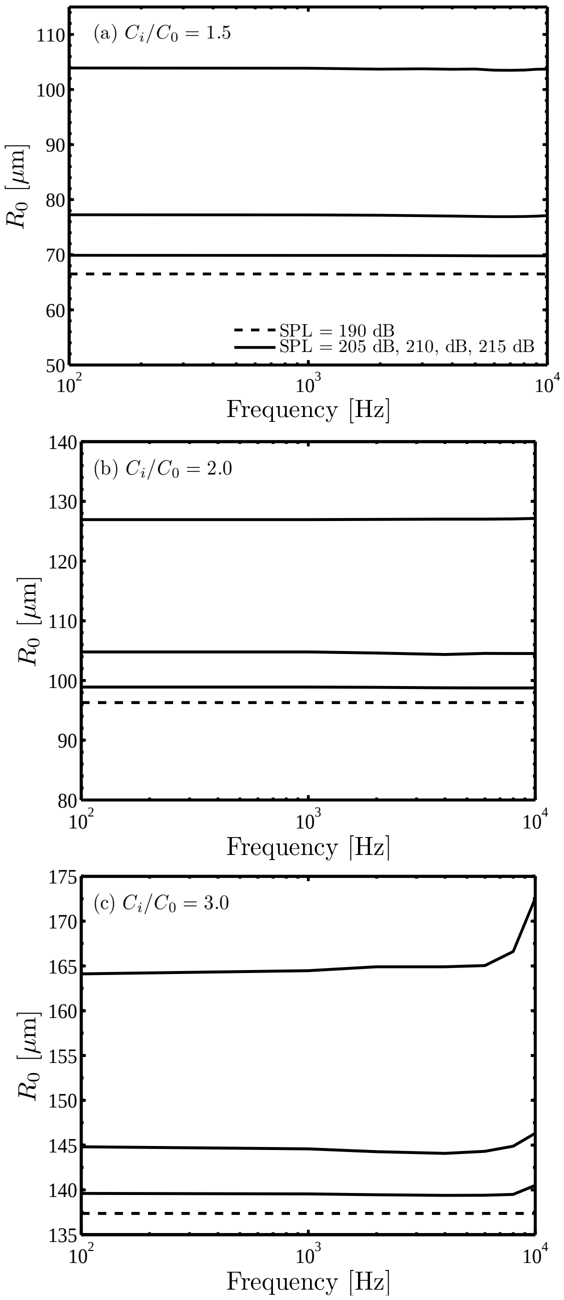

Figure 4.8: Equilibrium radius after 100 s versus driving frequency. Each plot contains data for SPL = 190 dB, 205 dB, 210 dB, and 215 dB. Plots (a)–(c) show $R_0(t_f)$ for C_i/C_0 = 1.5, 2.0, and 3.0 respectively.

creases. Figure 4.9 shows η as a function of R_0 calculated using Eq. (2.15) for f = 100 Hz, 1 kHz, 10 kHz, and 100 kHz. As shown in Fig. 4.9, increased drive frequency and bubble radius increase the polytropic index, which leads to less heat exchanged between the bubble and the fluid. Since η increases as R_0 increases, f_0 will increase as well.

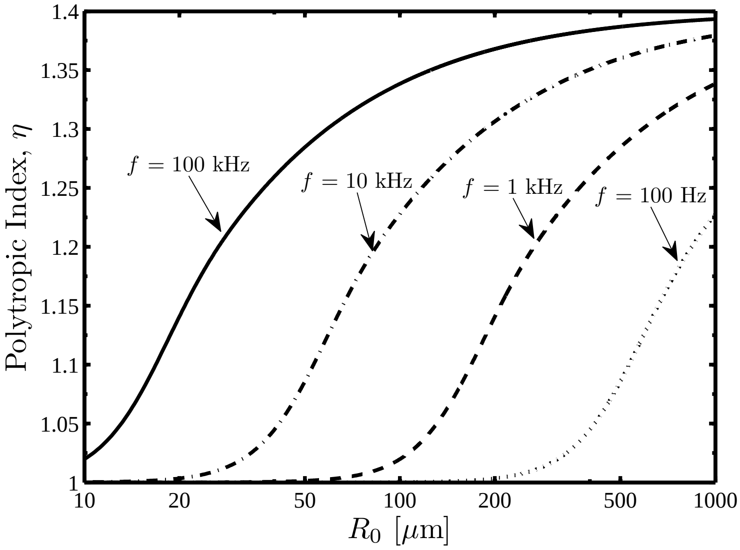

Figure 4.9: Polytropic index as a function of R_0. The driving frequency ranges from 100 Hz to 100 kHz.

Figure 4.10 examines how gas supersaturation affects $R_0(t)$. The initial equilibrium radius is 10 μm. Respectively, the columns contain data for f = 100 Hz, 10 kHz, 100 kHz. The rows contain data for C_i/C_0 = 1.5, 2.0, and 3.0 . Each plot shows $R_0(t)$ for static diffusion and SPL = 215 dB. For f = 100 Hz and 10 kHz, there is no difference in $R_0(t)$ curves except for $C_i/C_0 = 3.0$ (as shown in Fig. 4.8). When f = 100 kHz, the growth rate for a

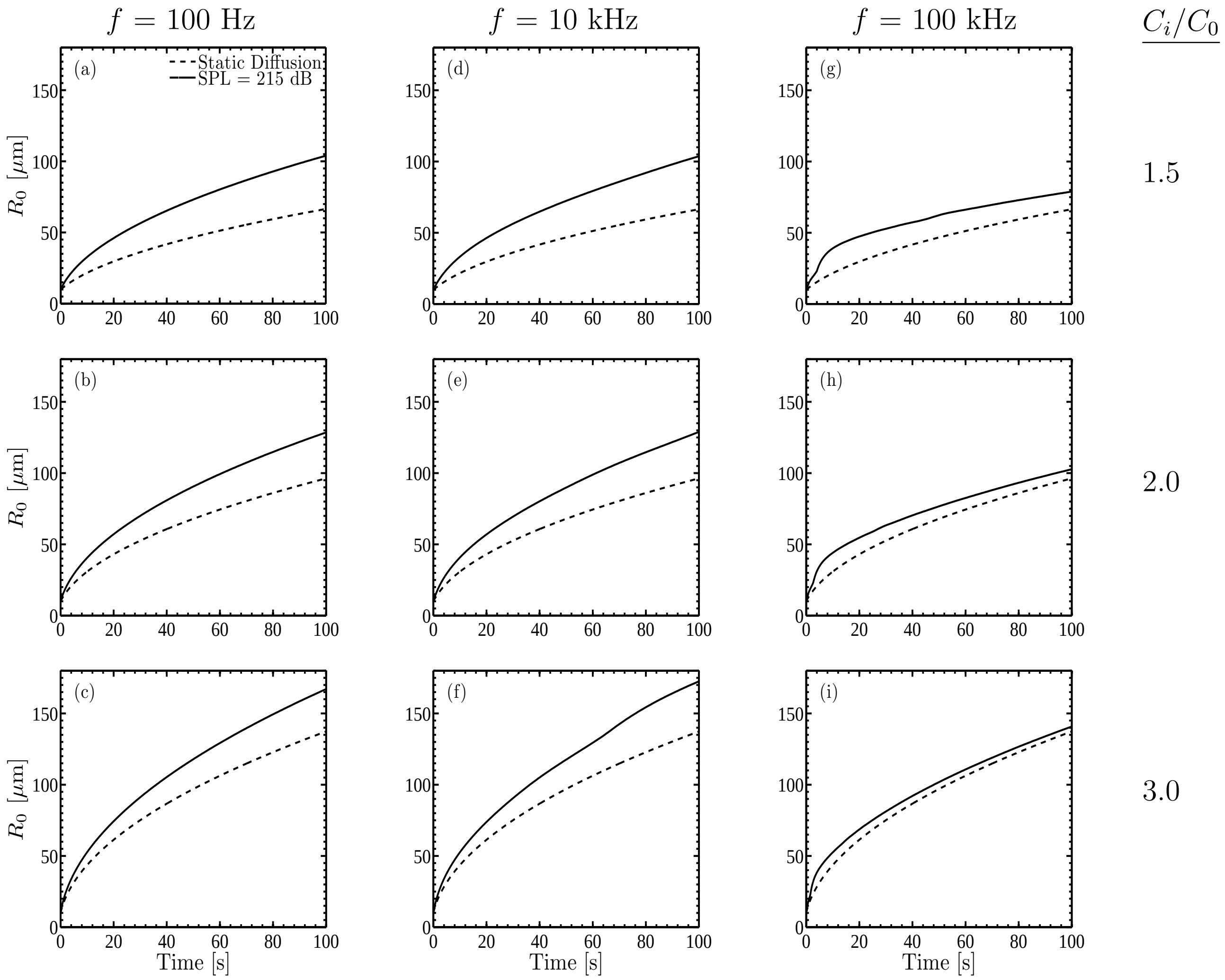

Figure 4.10: Equilibrium bubble radius versus time for several supersaturations, driving frequencies, and for static diffusion as well as SPL = 215 dB. From left to right, the columns show $R_0(t)$ for f = 100 Hz, 10 kHz, and 100 kHz. From top to down, the rows contain $R_0(t)$ for C_i/C_0 = 1.5, 2.0, and 3.0. Each plot contains $R_0(t)$ for static diffusion and SPL = 215 dB.

bubble driven at SPL = 215 dB is approximately equal to the growth rate during static diffusion after the bubble passes through resonance. Figure 4.10(g)–(i) shows this relation to be true for all three supersaturations. When gas supersaturation is increased, a similar relation shown in Fig. 4.6 repeats itself. Figure 4.11 contains the percent increase in R_0 relative to $C_i/C_0 = 1.5$ for $C_i/C_0 = 2.0$ and 3.0. In Fig. 4.11(a), the percent increase in $R_0(t)$ is shown for static diffusion. After an initial period of growth, the percent increase in R_0 is constant relative to $C_i/C_0 = 1.5$. Interestingly, when C_i/C_0 is doubled from 1.5 to 3.0, the percent increase in R_0 is 105%, or R_0 is slightly more than doubled. When C_i/C_0 increases by 33% from 1.5 to 2.0, the increase in R_0 is more than 40%. Figure 4.11(b) shows the percent increase in R_0 as the SPL is increased to 215 dB. The percent increase in R_0 is less for SPL = 215 dB than the static diffusion case.

4.2 Bubble growth due to Sonar Signals

The potential connection between marine mammal strandings and sonar testing merits the investigation of bubble growth due to sonar signals.[1,3–6,8,10] First, bubble growth due to monofrequency sonar signals is discussed, and then bubble growth data when excited by a sonar signal using frequency sweeps is presented.

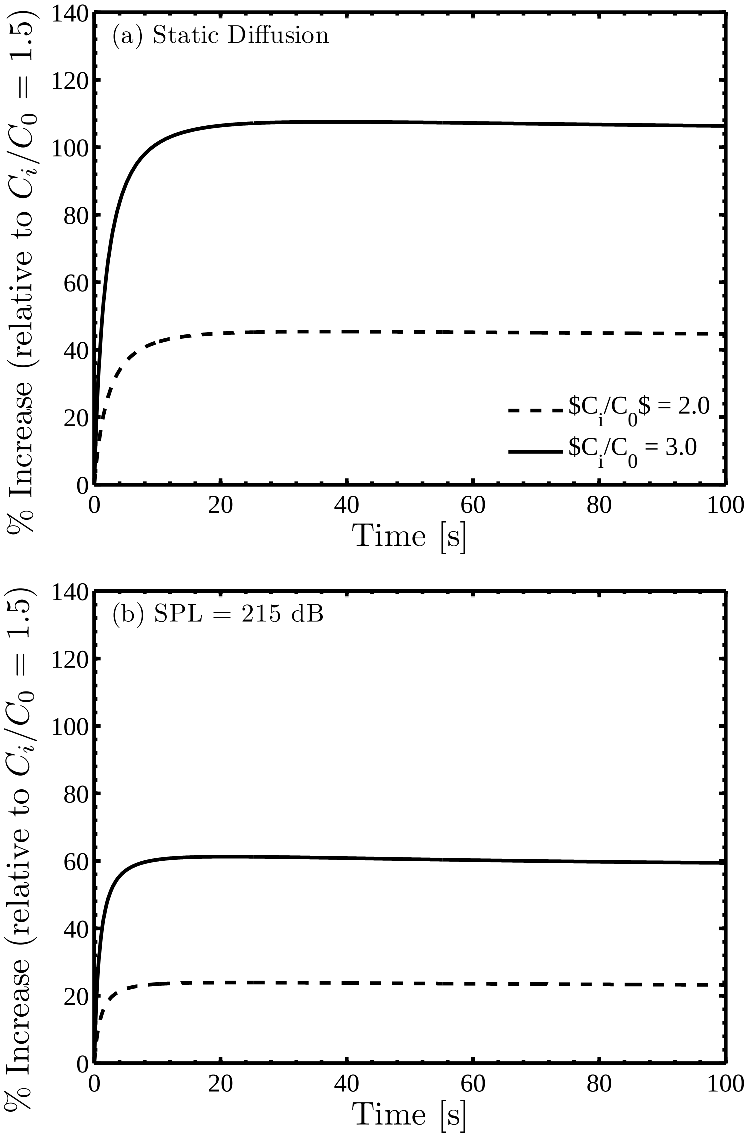

Figure 4.11: Percent increase in R_0 relative to static diffusion for $R_{00} = 10$ μm and $f = 1$ kHz. Plot (a) shows the percent increase in R_0 with $C_i/C_0 = 1.5$ for static diffusion and (b) shows the percent increase in R_0 with $C_i/C_0 = 1.5$ for SPL = 215 dB.

4.2.1 Monofrequency Sonar Source

A bubble exposed to a sonar signal is not insonified continuously. We define the sonar period as T_s. During T_s, the percentage of time for which the bubble is insonified is the duty cycle:

$$\mathrm{DC} = \frac{T_{\mathrm{on}}}{T} \times 100\%, \tag{4.7}$$

where T_{on} is the insonification time during the sonar period. During insonification, the bubble grows via rectified diffusion. The bubble will grow via static diffusion when it is not insonified. In Fig. 4.12, $R_0(t)$ is shown for a bubble driven at SPL = 215 dB, $f = 1$ kHz, $T_s = 10$ s, and DC = 10%, 20%, and 50%. The upper limit for bubble growth is continuous insonification (DC = 100%) and lower limit is static diffusion. The curves for $R_0(t)$ are stacked in increasing order of duty cycle. Figure 4.12(a) shows $R_0(t)$ for a gas supersaturation of 150%. The intervals of rectified diffusion and static diffusion are apparent in Fig. 4.12(a). As the duty cycle increases, rectified diffusion occurs for a longe period during T_s which causes greater bubble growth. Figure 4.12(b) displays $R_0(t)$ for an increased gas supersaturation of 300%. As C_i/C_0 increases, static diffusion becomes more prominent which makes the time intervals during static diffusion and rectified diffusion less apparent.

Bubble growth due to a gated sonar source and continuous insonification can be related by considering the work done on a bubble by the acoustic source. The sound power level is defined as

$$\mathrm{PWL} = 10 \log_{10} \frac{W}{W_{\mathrm{ref}}}. \tag{4.8}$$

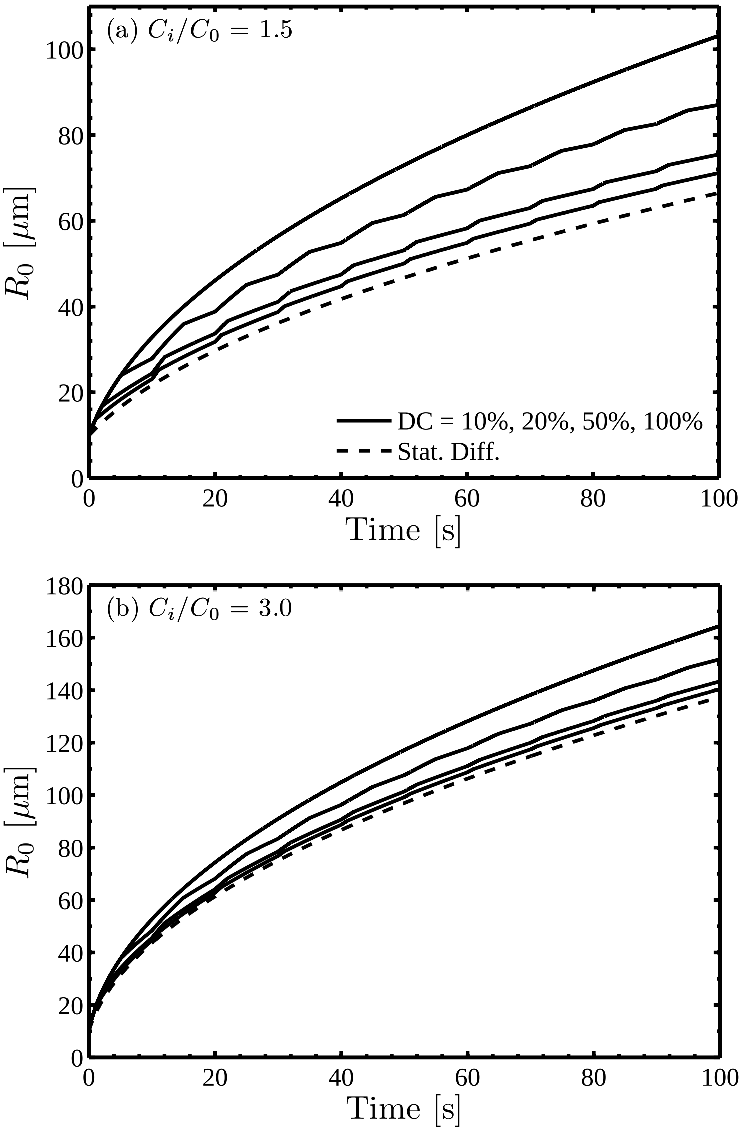

Figure 4.12: $R_0(t)$ for $f = 1$ kHz, SPL $= 215$ dB, $T_s = 10$ s, and DC $= 10\%$, 20%, 50%, and 100%. The top curve in each plot is continuous insonification (DC $= 100\%$) and the bottom curve is static diffusion. Plot (a) contains data for $C_i/C_0 = 1.5$ and plot (b) contains data for $C_i/C_0 = 3.0$. As C_i/C_0 increases, the periods of static diffusion and rectified diffusion are less apparent.

If PWL is taken over a sonar period T_s, then the amount of work done on the bubble is the percentage of insonification during the sonar period or the duty cycle. To calculate the loss in decibels as a function of duty cycle, we use the following equation:

$$L_{\mathrm{DC}} = 10\log_{10}\frac{\mathrm{DC}\times W}{W_{\mathrm{ref}}} - 10\log_{10}\frac{W}{W_{\mathrm{ref}}} = 10\log_{10}\mathrm{DC}. \tag{4.9}$$

Since the duty cycle is less than unity, L_{DC} will be negative. The bubble still grows during static diffusion, thus Eq. (4.9) does not account for all of the bubble growth. If 1 dB (which roughly accounts for growth due to static diffusion) is added to Eq. (4.9), an equation for $R_0(t)$ for sonar signals approximates $R_0(t)$ for continuous insonification at a lower SPL:

$$L_{\mathrm{DC}} = 1 + 10\log_{10}\mathrm{DC}. \tag{4.10}$$

Results from Eq (4.10) are in Fig. 4.13(a) for $C_i/C_0 = 1.5$ and (b) for $C_i/C_0 = 3.0$. The plots contain data for f = 1 kHz and SPL = 215 dB. When $C_i/C_0 = 1.5$, Eq. (4.10) agrees well with the data until DC = 45%. As the duty cycle increases to 100%, Eq. (4.9) is no longer valid. Equation (4.10) predicts that the equivalent SPL for a continuous wave source would be 1 dB higher than the sonar signal with DC = 100%, which is an inconsistent result. Or, Eq. (4.10) predicts that continuous insonification at two different SPLs (215 dB and 216 dB) yields the same final equilibrium radius, which is not possible when a bubble is forced above the threshold for rectified diffusion. The data points in Fig. 4.12(b) do not agree with Eq. (4.10) for DC $<$ 5% because the correction term of 1 dB in Eq. (4.10) was estimated for $C_i/C_0 = 1.5$. But, as

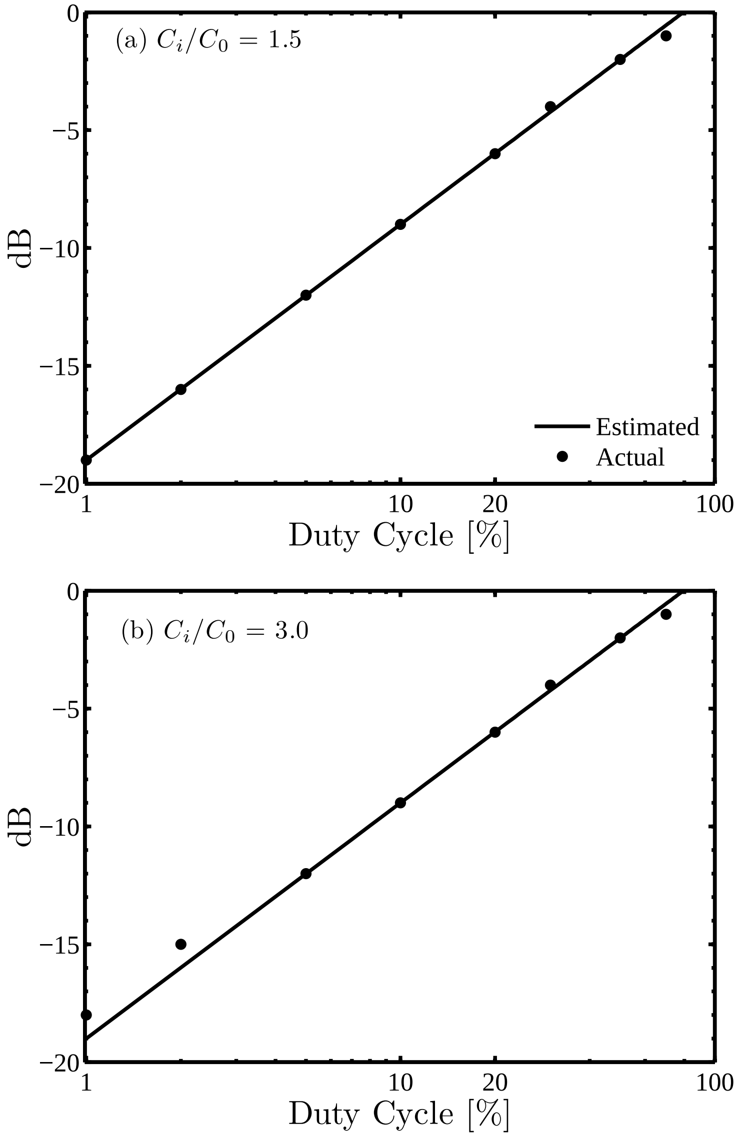

Figure 4.13: Decibels down from 215 dB for a continuous wave source as a function of duty cycle for (a) $C_i/C_0 = 1.5$ and (b) $C_i/C_0 = 3.0$. The data points were obtained by matching $R_0(t_f)$ for a duty cycle to $R_0(t_f)$ at a lower SPL. The log relation is calculated using Eq. (4.10). The driving frequency is 1 kHz.

DC increases, Eq. (4.10) agrees with the data points. Similar to the case of $C_i/C_0 = 1.5$, Eq. 4.10 does not correctly predict the loss in decibels for a sonar signal as the duty cycle increases to 100%.

4.2.2 Bubble Growth for Frequency Sweeps

Bubble growth was also simulated for a model sonar signal composed of swept sinusoids. The sonar signal we present consists of four segments: two Hyperbolic Frequency Modulation (HFM) sweeps, a segment of monofrequency excitation, and a segment with no sound. To obtain maximum bubble growth, both the maximum duty cycle and maximum periods of insonification were used. The duty cycle is 20% and the period of insonification is 2.5 s.

The acoustic signal during an HFM sweep is

$$s(t) = w(t)\sin\left[a\ln\left(1-kt\right)\right],\ \text{for } 0 \le t \le T, \tag{4.11}$$

where $w(t)$ is the windowing function. The argument of the sine function determines the instantaneous frequency:

$$k = \frac{f_2 - f_1}{f_2 T}, \tag{4.12}$$

$$a = -\frac{2\pi f_1 f_2}{f_2 - f_1}T, \tag{4.13}$$

where f_1 is the initial frequency, f_2 is the final frequency, and T is the pulse duration. The windowing function $w(t)$ is calculated by

$$w(t) = \begin{cases} \sin^2\left(\frac{\pi t}{2T_w}\right) & \text{for } 0 \le t \le T_w \\ 1 & \text{for } T_w \le t \le T - T_w \\ \sin^2\left[\frac{\pi}{2}\frac{t-(T-T_w)}{T_w}\right] & \text{for } T - T_w \le t \le T \end{cases} \tag{4.14}$$

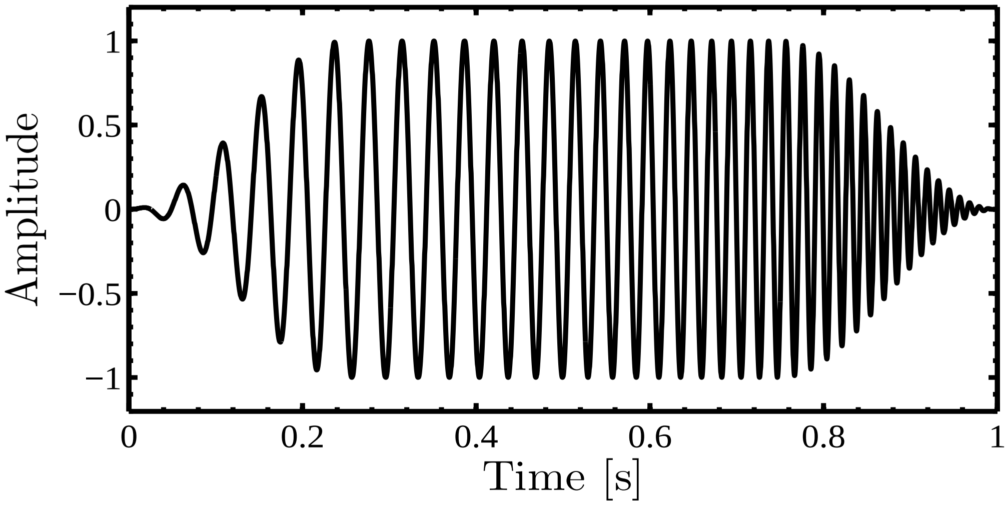

Figure 4.14: An HFM source for $f_1 = 20$ Hz, $f_2 = 100$ Hz, $T_\mathrm{w} = 0.25$ s, and $T = 1$ s.

Figure 4.14 displays an HFM source for $f_1 = 20$ Hz, $f_2 = 100$ Hz, $T_w =$ 0.25 s, and $T = 1$ s. The frequency parameters used in Fig. 4.14 facillitate illustration of the signal in the time domain. For bubble growth calculations in this thesis, the driving frequency ranged from 2536 Hz to 4268 Hz. Both the model sonar signal and the parameters used for the signal are in Fig. 4.15 and Table 4.3, respectively.

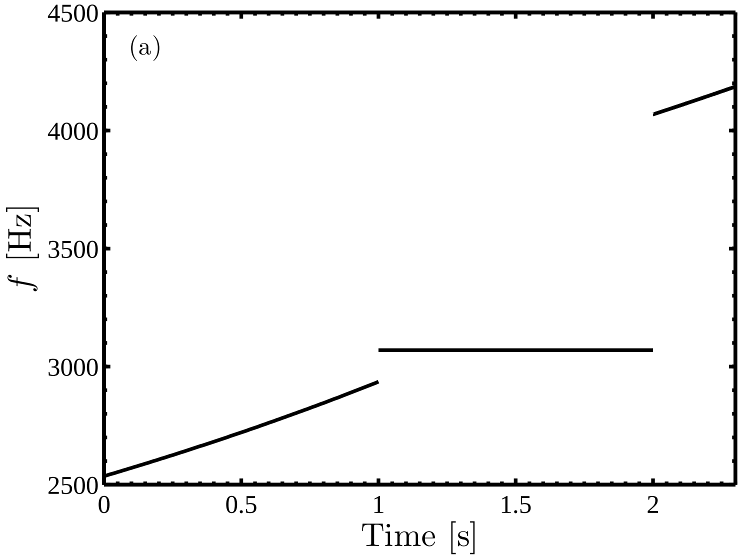

Figure 4.15: Frequency versus time for two HFM sweeps and monofrequency excitation. Refer to Table 4.3 for parameter values.

Time, t [s]	frequency, f [Hz]
$0 \leq t < 1$	$2536 \leq f \leq 2936\ Hz$
$1 \leq t < 2$	$f = 3070$
$2 \leq t < 2.5$	$4068 \leq f \leq 4268\ Hz$

Table 4.3: Frequency versus time for model sonar signal in Fig. 4.15.

To calculate bubble growth for the frequency signal in Fig. 4.15, we set

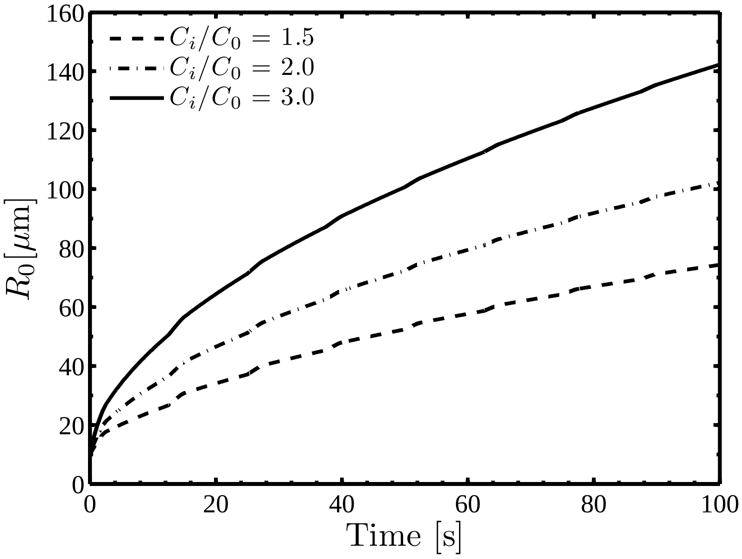

Figure 4.16: Equilibrium radius for a bubble driven by the frequency signal in Fig. 4.15 at SPL = 215 dB, $C_i/C_0 = 1.5$, 2.0, and 3.0, $T_s = 12.5$ s, and DC = 20%.

the sonar period $T_s = 12.5$ s, the duty cycle DC = 20%, and thus $T_{\mathrm{on}} = 2.5$ s. Figure 4.16 shows $R_0(t)$ for a bubble driven at SPL = 215 dB for $C_i/C_0 = 1.5$, 2.0, and 3.0. The final equilibrium radius $R_0(t_f)$ for all three gas supersaturations are within 1% of $R_0(t_f)$ driven at 215 dB for $f = 1$ kHz and DC = 20%. For monofrequency sources, Fig. 4.8 shows that $R(100)$ is approximately constant from 100 Hz to 10 kHz when $R_{00} = 10$ μm. Therefore, the frequency sweeps do not alter bubble growth for the driving frequencies, gas supersaturations, and bubble sizes discussed. Consequently, the equivalent SPL for a duty cycle of 20% driven by the frequency signal in Fig. 4.14 is 209 dB.

4.3 Modelling Bubble Growth in Stranded Marine Mammals

Considerable media attention has focused on marine mammal stranding events coinciding with mid-frequency sonar (f = 1–10 kHz) tests.[1,3–6,8] Although no known mechanism has been determined for causing the strandings, one possibility considered is that sonar might induce decompression sickness.[8] Gas supersaturation approaching 300% has been estimated in dolphins after a dive series.[14] At these supersaturation levels, a pressure fluctuation, for instance from an acoustic pressure source, can lead to cavitation of previously stabilized bubble nuclei. Once perturbed from equilibrium conditions, the bubble can grow by rectified diffusion or static diffusion. In 2007, Crum et al.[10] investigated the potental for bubble nucleation in supersaturated *ex vivo* bovine blood, liver, and kidneys when exposed to a 37 kHz source. The study found that nucleaction occured only for supersaturated tissue and that nucleation occured for pressure amplitudes as low as 50 kPa (SPL = 211 dB). Although the experiments used frequencies well above those used by mid-frequency sonar, the physics behind the growth mechanisms is similar.

For our model, it is assumed that: bubble growth is not bounded by tissue, bones, etc.; the bubble is in infinite, supersaturated water; surface tension acts on the bubble; bubble growth occurs after a pressure disturbance from an acoustic field; and the bubble does not have surfactants. Although the simplifications are many, we are primarily concerned with rapid bubble growth after the bubble has been activated by a pressure source. In Fig. 4.17, $R_0(t)$ is shown for a marine mammal that has surfaced after being driven by a sonar signal. We assume that the marine mammal is at a sufficient distace from the sonar signal such that static diffusion is the primary growth mechanism (SPL $<$ 205 dB). The pressure in the muscle tissue due to nitrogen is calculated using Eq. (2.2) with $v_p = 0$ Pa/s:

$$p_n = p_{ag} + e^{-t/\tau_w} \left(p_0 - p_{ag}\right). \tag{4.15}$$

The alveolar gas p_{ag} is at atmospheric pressure and the term p_0 is the initial pressure in the tissue due to supersaturation. Gas pressure can be put in terms of gas concentration using Henry's law. The marine mammal surfaces with supersaturated tissue, but it is breathing air at atmospheric pressure and the supersaturation level within the tissue will decrease over time. Initial gas supersaturation ratios are 1.5, 2.0, and 3.0. As time progresses, the gas concentration C_r adjacent to the bubble wall, Eq. (2.5), will be greater than the gas concentration C_i in the tissue far from the bubble. At this point in time, the concentration gradient is caused by surface tension. The ratio C_i/C_0 decreases over time, and thus bubble growth will be less than if C_i/C_0 was constant. For all three initial gas supersaturations shown in Fig. 4.17, the bubble starts to dissolve after $t = 0.4$ hr or 24 min. Embolism and tissue separation can occur when *in vivo* bubbles are on the order of ten microns.[14] The data in Fig. 4.17 predicts that a marine mammal could potentially suffer from decompression sickness since bubbles can grow to 60 μm in 30 s for $C_i/C_0 = 3.0$. Of interesting note, necropsy results of Cuvier beaked whales from a stranding event in the Canary Islands in 2002 found tissue and organ trauma consistent with damage caused by rapid decompression (i.e., decompression sickness).[8]

Figures 4.18(a), (c), and (e) show potential equilibrium radii versus time if a marine mammal surfaced and is being driven by $f = 1$ kHz, which is within the mid-frequency sonar range. To prevent harming marine mammals and sea turtles by U.S. Navy Surveilance Towed Array Sensor System Low Frequency ($f = 100$–500 Hz) Active Sonar (SURTASS), the U.S. Navy employs monitoring and mitigation measures.[31] If a marine mammal is approaching the mitigation zone (typically 1 km radially away from the source), then the U.S. Navy suspends sonar testing. At the border of the mitigation zone, the SPL is 180 dB maximum, which is below the level that can induce significant bubble growth from rectified diffusion. Although the driving frequency used for the calculations is above SURTASS LFA levels, the flat response of $R_0(t)$

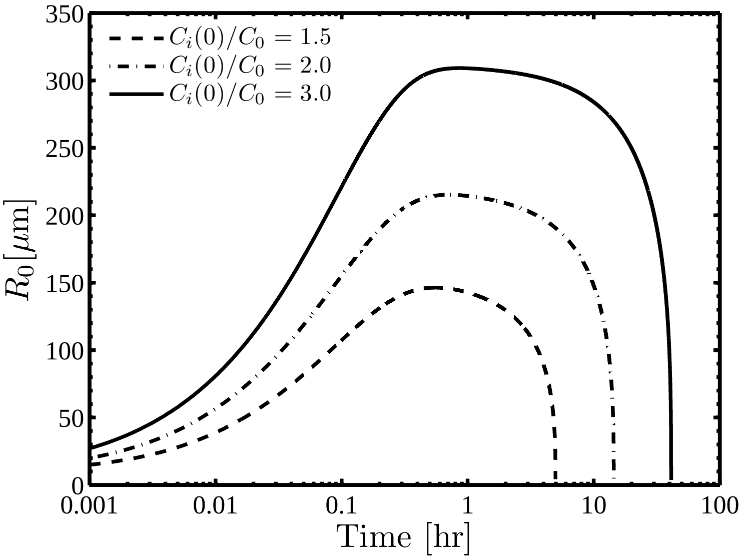

Figure 4.17: Equilibrium radius versus time for a marine mammal that has surfaced with initial supersaturated levels of 1.5, 2.0, and 3.0. Bubble growth is caused by static diffusion. Equation (2.2) is used to calculate the nitrogen pressure in muscle tissue with $v_p = 0$ Pa/s.

for frequencies ranging from 100 Hz–10 kHz means that the increased driving frequency will not alter bubble growth for our model. If naval mitigation efforts are successful, then bubble growth due to rectified diffusion will not occur. But, we present the simulation data as a possible scenario. Figures 4.18(b), (d) and (f) display $C_i(t)/C_0$ for initial concentration ratios of 1.5, 2.0, and 3.0 respectively.

Although SURTASS LFA sonar signals last from 6 s–100 s with passive periods of 6 min–15 min,[31] Fig. 4.18 contains data for bubble growth during 60 min of insonification, Similar to data in Fig. 4.18, bubble growth will be less than growth for a constant gas supersaturation since the ratio $C_i(t)/C_0$ decreases over time. But, the SPL is above the threshold for rectified diffusion, and thus rectified diffusion will sustain bubble growth after the muscle tissue is saturated $C_r > C_i$). Table 4.3 shows that significant bubble growth can occur after 30 s for the lowest SPL and C_i/C_0. Of interest, a bubble that is driven at SPL = 205 dB does not experience significant growth relative to static diffusion for the first minute. As time progresses and C_i/C_0 approaches 1.0 ($t \approx 24$ min), and rectified diffusion becomes the mechanism driving bubble growth. For SPL = 215 dB, the equilibrium radius experiences rapid bubble growth for all three initial supersaturations. It is highly unlikely that a marine mammal will be exposed to 215 dB because a marine mammal would have to be in the immediate proximity of the sonar source, and whales have shown avoidance to intense, industrial anthropogenic sound.[32]

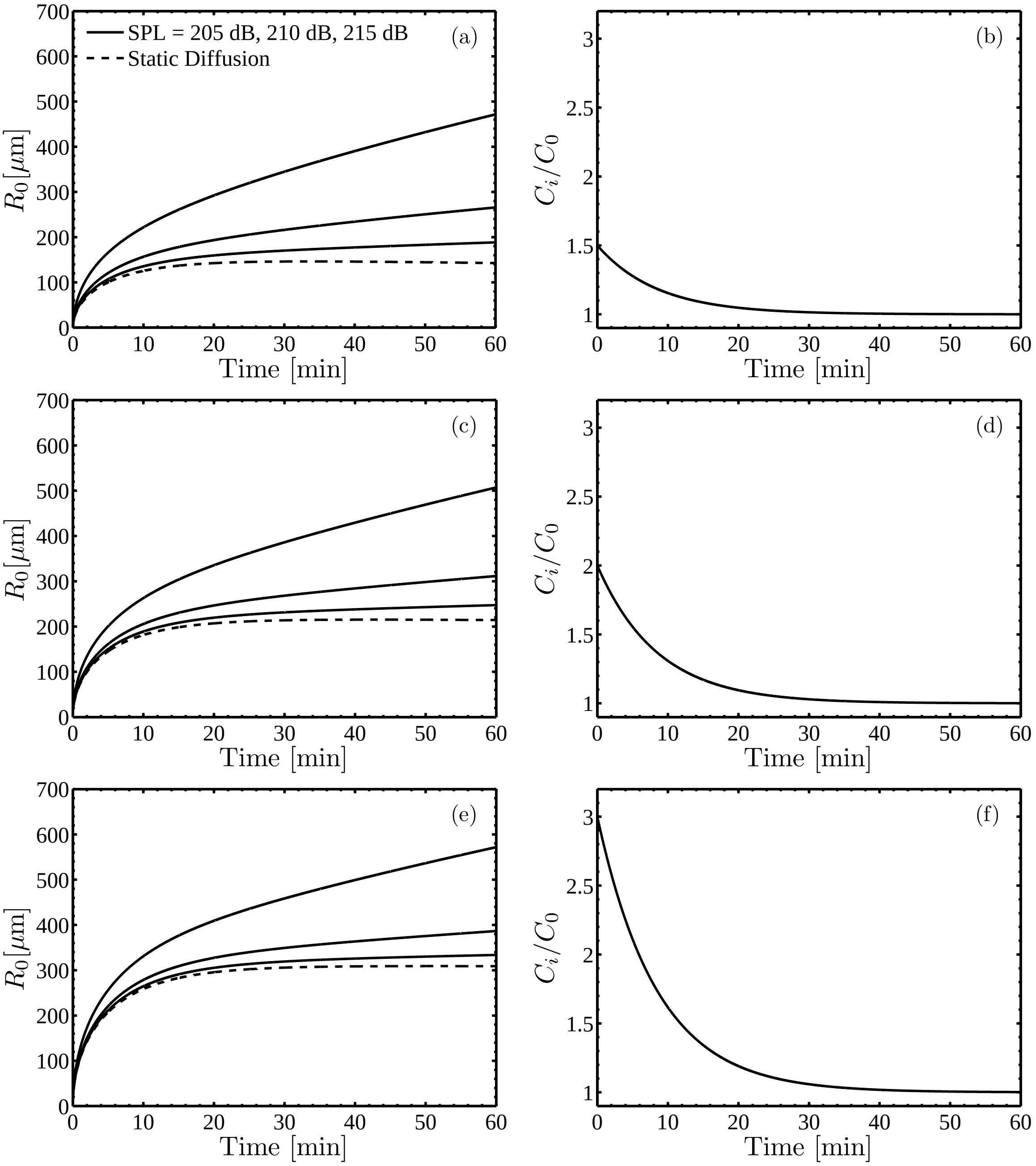

Figure 4.18: Equilibrium radius versus time and $C_i(t)/C_0$ for $f = 1$ kHz, static diffusion and SPL = 205 dB, 210 dB, and 215 dB. The rows contain data for $C_i(0)/C_0 = 1.5$, 2.0, and 3.0.

		$R_0(t)$ [μm]		
Time [s]	SPL [dB]	$C_i(0)/C_0 = 1.5$	$C_i(0)/C_0 = 2.0$	$C_i(0)/C_0 = 3.0$
30	0	35.58	51.80	73.99
	205	37.45	53.24	75.20
	210	41.51	56.46	78.02
	215	55.98	69.22	89.91
60	0	49.62	72.22	103.2
	205	52.31	74.27	104.9
	210	58.14	78.92	109.0
	215	78.81	97.03	125.5

Table 4.4: Equilibrium radius at 30 s and 60 s for: $C_i(0)/C_0 = 1.5$, 2.0, and 3.0; SPL = 205 dB, 210 dB, and 215 dB; and $f = 1$ kHz.

Chapter 5

Conclusion

In this thesis, bubble growth has been modelled via rectified and static diffusion for driving frequencies ranging from 100 Hz to 100 kHz, for SPLs up to 215 dB, and for gas supersaturation levels up to 300%. The primary intention was to extend the results of Crum and Mao[12] on bubble growth via rectified diffusion, using gas supersaturation levels estimated in marine mammals by Houser et al.,[14] which were significantly higher than those used by Crum and Mao. Interest in this matter was sparked after several stranding events coincided with exercises of high intensity, mid-frequency active sonar.[4–6,8] As a consequence of these strandings, significant public, legal, and national defense interest has been atuned to the issue.[1,33,34] The U.S. Court of Appeals for the 9th circuit made a ruling to place restrictions on U.S. Naval sonar testing.[33] But, in November 12, 2008, the Supreme Court overruled the decision made by the 9th circuit, thereby allowing the U.S. Navy to conduct warfare training unhindered.[35] The ultimate goal for work of this type is to investigate the hypothesis that strandings could be related to decompression sickness under the influence of bubble growth by rectified diffusion. Full evaluation of this hypothesis is beyond the scope of this thesis. The focus here is on idealized mathematical simulation of bubble growth in a fluid medium of supersaturation levels predicted to occur in marine mammals[14] and insonified by sonar-like signals.

Bubble growth was mathematically simulated for continuous, monofrequency insonification as well as for pulsed sonar signals using monofrequency excitation and frequency sweeps. In our model, bubble growth was simulated in an infinite, incompressible heat reservoir of supersaturated water. Surface tension acts on the bubble and thermal damping, shear viscosity, and radiation losses during polytropic oscillations were considered. The equations used to model bubble growth were reviewed in Chapter 2. A form of the Rayleigh-Plesset equation[12] was used to calculate the instantaneous bubble radius R, and the Fyrillas-Szeri equation[17] was used to determine the equilibrium radius R_0.

In Chapter 3, the numerical models used to determine bubble growth were reviewed. To calculate changes in the equilibrium radius of an insonified bubble, the Rayleigh-Plesset equation was integrated to determine the time-dependent bubble radius for 10 to 20 acoustic cycles. The results were used to evaluate the time averages in Eqs. (3.3), (3.4), and (3.14). Using these time averages, the Fyrillas-Szeri equation was integrated for 0.5 s to 1.0 s and a new equilibrium radius is calculated. This algorithm was repeated for a sufficient number of times to determine the equilibrium radius R_0 at the end of the desired time interval. Integration of the Rayleigh-Plesset equation and the Fyrillas-Szeri equation was performed by an adaptive, fourth-order Runge-Kutta method.[27] To confirm the model's validity, results were compared with those previously published in the literature.[12,18]

In Chapter 4, bubble growth for continuous sources and sonar signals was discussed. Bubble growth for conditions similar to those found in supersaturated, marine mammal muscle tissue was estimated. Rectified diffusion was significant for sound pressure levels greater than 205 dB. For monofrequency, continuous sources there is negligible variation in $R_0(t)$ for 100 Hz to 10 kHz after 100 seconds of insonificaion for an initial bubble radius of 10 μm. Bubble growth due to gated sonar signals was related to an equivalent SPL for continuous insonification with Eq. (4.10). It was determined that frequency sweeps in sonar signals for 100 Hz through 10 kHz do not significantly increase bubble growth beyond growth by static diffusion, as was found for continuous wave sources. Mitigation efforts of the U.S. Navy[31] limit the possibility for bubble growth due to rectified diffusion because the source levels within the mitigation zone are below those which can cause significant growth by rectified diffusion. But, sonar signals could possibly activate nuclei within supersaturated muscle tissue[10] and cause bubble growth due to static diffusion.

As gas supersaturation increases, static diffusion is the dominant bubble growth mechanism for bubbles on the order of microns and being forced by frequencies ranging from 100 Hz to 10 kHz (see Table 4.1). For a frequency of 1 kHz, more bubble growth occurs when the gas supersaturation is 300% with no sound than when the gas supersaturaion is 150% with SPL = 215 dB. The percent growth for a bubble from no sound to SPL = 215 dB is 57% for a gas supersaturation of 150% and 20% for a gas supersaturation of 300%.

Uncharacteristic strandings of Cuvier's beaked whales[4] during sonar testing and visual evidence of decompression sickness in stranded Cuvier's beaked whales[8] has generated concern about the possibility of sonar leading to strandings caused by decompression sickness. If bubble growth determined in this thesis occurs *in vivo*, then embolism and other damage due to decompression sickness may occur. To determine the possibility of this scenario, more accurate models for *in vivo* bubble growth are essential. Investigations into the stabilization and activation of *in vivo* nuclei need to be explored. A more accurate model for gas diffusion, such as the model designed by Ilinskii et al.,[18] should be implemented. It is imperative that the environment surrounding the bubble reflects the *in vivo* environment, and the influence of bubble surfactants is included. In addition, behavioral and physiological responses of marine mammals to intense sounds could increase the levels of gas supersaturation and exacerbate bubble growth. Finally, experimentation with tissue *in vitro* and *in vivo* would be required to ultimately prove the existance of bubble growth.

Appendix

Alternate Derivation of Mass Transfer Rate for a Bubble due to Static Diffusion

As stated in Sec. 2.2, to describe mass transport in a liquid, Epstein and Plesset[19] used Fick's Law for mass transfer in a spherical-symmetric geometry:

$$\frac{\partial C}{\partial t} = \frac{D}{r^2}\frac{\partial}{\partial r}\left(r^2\frac{\partial C}{\partial r}\right). \tag{1}$$

The physical setup of the problem will be the same as previously stated in this paper. The initial condition and boundary conditions are

$$\begin{aligned} C(r,0) &= C_i\,, \quad r > R_0\,, \\ \lim_{r\to\infty} C(r,t) &= C_i\,, \\ C(R_0,t) &= C_R\,. \end{aligned} \tag{2}$$

The following derivation[21] outlines the steps leading to the result obtained by Epstein and Plesset. To simplify this problem, it is convenient to perform the following change of variables: $\phi/r = C - C_i$. The diffusion equation simplifies to

$$\frac{\partial \phi}{\partial t} = D\frac{\partial^2 \phi}{\partial t^2}, \tag{3}$$

which has the familiar form of a 1-D diffusion equation in cartesian coordinates. The boundary conditions are now $\phi(R_0,t) = (C_R - C_i)\,R_0$, and as $r \to \infty, C(r,t) = 0$.

Performing a Laplace transform on ϕ yields

$$s\tilde{\phi} = D\frac{\partial^2 \phi(\tilde{r}, s)}{\partial r^2}. \tag{4}$$

The boundary conditions become $\tilde{\phi}(R_0, s) = (C_R - C_i)\, R_0/s$ and $\tilde{\phi}\,(\infty, s) = 0$. When solving for ϕ, one finds

$$\phi(r, s) = \frac{(C_R - C_i)\, R_0}{s} e^{-\sqrt{s/D}(r-R_0)}. \tag{5}$$

Taking the inverse transform, and recasting in terms of gas concentration produces

$$C = C_i + \frac{1}{r}\,(C_R - C_i)\, R_0 \mathrm{erfc}\frac{r - R_0}{2\sqrt{Dt}}. \tag{6}$$

Based on results from Epstein and Plesset, gas concentration can be related to mass exchange rate:

$$\frac{dm_b}{dt} = M\frac{dn_b}{dt} = 4\pi R_0^2 DM\frac{\partial C}{\partial r} = 4\pi R_0^2 DM\,(C_i - C_R)\left(\frac{1}{R_0} + \frac{1}{\sqrt{\pi Dt}}\right), \tag{7}$$

where m_b is the mass of the gas inside the bubble and M is the molecular weight of the gas. Since $C_R = C_0\,(1 + 2\sigma/p_0 R_0)$, it follows that

$$\frac{dm_b}{dt} = 4\pi R_0^2 D C_0 M\left[\frac{C_i}{C_0} - \left(1 + \frac{2\sigma}{p_0 R_0}\right)\right]\left(\frac{1}{R_0} + \frac{1}{\sqrt{\pi Dt}}\right). \tag{8}$$

From this equation, it is evident that the solution needs to be supersaturated to prevent the bubble from dissolving. This is because of the excess pressure in the bubble due to surface tension. If surface tension is negligible, then the solution needs to at least be saturated to stop dissolution. The result coincides exactly with the expression found in Epstein and Plesset:[13]

$$\frac{dm_b}{dt} = 4\pi R_0^2 D C_0 \left[\frac{C_i}{C_0} - \left(1 + \frac{2\sigma}{p_0 R_0} \right) \right] \left(\frac{1}{R_0} + \frac{1}{\sqrt{\pi D t}} \right), \tag{9}$$

where here concentration is measured in kilograms per unit volume.

Bibliography

[1] Marine Mammal Commission, "Marine mammals and noise, a sound approach to research and manangement," A report to Congress from the Marine Mammal Commission, March 2007.

[2] M. C. Hastings, "Coming to terms with the effects of ocean noise on marine animals," Acoustics Today **4**, 22-34 (2008).

[3] J. A. Hildebrand, "Impacts of anthropogenic sound" in J. E. Reynolds et al. (eds.), Marine Mammal Research: Conservation beyond Crisis. The Johns Hopkins University Press, Baltimore, Maryland. pages 101-124 (2005).

[4] A. Frantzis, "Does acoustic testing strand whales?," Nature **392**, 29 (1998).

[5] D. I. Evans and G. R. England, "Joint interim report/Bahamas marine mammal stranding event of 15-16 March 2000," National Oceanic and Atmospheric Administration, U.S. Dept. of Commerce and U.S. Navy, Washington, DC, 61 pages (2001).

[6] D. R. Ketten, "Beaked whale necropsy findings for strandings in the Bahamas, Puerto Rico, and Maderia, 1999–2002," Woods Hole Oceanog. Inst. Tech. Rept., WHOI-2005-09.

[7] T. M. Cox, T. J. Ragen, A. J. Read, E. Vos, R. W. Baird, K. Balcomb, J. Barlow, J. Caldwell, T. Cranford, L. Crum, A. D'Amico, G. D'Spain,

A. Fernandez, J. Finneran, R. Genty, W. Gerth, F. Gulland, J. Hildebrand, D. Houser, T. Hullar, P. D. Jepson, D. Ketten, C. D. Macleod, P. Miller, S. Moore, D. C. Mountain, D. Palka, P. Ponganis, S. Rommelo, T. Rowls, B. Taylor, P. Tyack, D. Wartzoki, R. Gisner, J. Meads, and L. Benner, "Understanding the impacts of anthropogenic sound on beaked whales," J. Cetacean Res. Manage. **7**, 177–187 (2006).

[8] P. D. Jepson, M. Arbelo, R. Deaville, I. A. P. Patterson, P. Castro, J. R. Baker, E. Degollada, H. M. Ross, P. Herrez, A. M. Pocknell, F. Rodrguez, F. E. Howie, A. Espinosa, R. J. Reid, J. R. Jaber, V. Martin, A. A. Cunningham, and A. Fernndez, "Gas-bubble lesions in stranded cetaceans," Nature **425** (2003).

[9] A. Fernández, J. F. Edwards, F. Rodriguez, A. Espinosa de los Monteros, P. Herraez, P. Castro, J. R. Jaber, V. Martin, and M. Arbelo, "Gas and fat embolic syndrome involving a mass stranding of beaked whales (family Ziphiidae) exposed to anthropogenic sonar signals," Vet. Pathology **42**, 446–457 (2005).

[10] L. A. Crum, M. R. Bailey, J. Guan, P. R. Hilmo, S. G. Kargl, and T. J. Matula, "Monitoring bubble growth in supersaturated blood and tissue ex vivo and the relevance to marine mammal bioeffects," Acoustics Research Letters Online **6**, 214–220 (2005).

[11] S. H. Ridgway and R. Howard, "Dolphin lung lollapse and intramuscular

circulation during free diving: evidence from nitrogen washout," Science **206**, 1182–1183 (1979).

[12] L. A. Crum and Y. Mao, "Acoustically enhanced bubble growth at low frequencies and its implications for human diver and marine mammal safety," J. Acoust. Soc. Am. **99**, 2898–2907 (1996).

[13] T. G. Leighton, *The Acoustic Bubble* (Academic, San Diego, 1994).

[14] D. S. Houser, R. Howard, and S. Ridgway, "Can diving-induced tissue nitrogen supersaturation increase the chance of acoustically driven bubble growth in marine mammals?" J. Theor. Biol. **213**, 183–195 (2001).

[15] A. Eller and H. G. Flynn, "Rectified diffusion during nonlinear pulsations of cavitation bubbles," J. Acoust. Soc. Am. **37**, 493–503 (1965).

[16] L. A. Crum, "Rectified diffusion," Ultrasonics **22**, 215-223 (1984).

[17] M. M. Fyrillas and A. J. Szeri, "Dissolution or growth of soluble spherical oscillating bubbles," J. Fluid Mech. **277** 381–407 (1994).

[18] Yu. A. Ilinskii, P. S. Wilson, and M. F. Hamilton, "Bubble growth by rectified diffusion at high gas supersaturation levels," J. Acoust. Soc. Am. **124**, 1950–1955 (2008).

[19] P. S. Epstein and M. S. Plesset, "On the stability of gas bubbles in liquid-gas solutions," J. Chem. Phys. **18**, 1505–1509 (1950).

[20] A. B. Lumb, *Nunn's Applied Respiratory Physiology*, 6th ed. (Elsevier, Philadelphia, 2006) Ch. 30, p. 399.

[21] Yu. A. Ilinskii, personal communications, August 2005–June 2007.

[22] R. E. Moon, R. D. Vann, and P. B. Bennett, "The physiology of decompression illness," Scientific American **273**, 70–75 (1995).

[23] L. A. Crum, "Measurements of the growth of air bubbles by rectified diffusion," J. Acoust. Soc. Am. **68**, 203-211 (1980).

[24] T. G. Leighton, "Derivation of the Rayleigh-Plesset equation in terms of volume," Tech. Report No. 308, Institute of Sound and Vibration Research, Jan. 2007.

[25] A. I. Eller, "Damping constants of pulsating bubbles," J. Acoust. Soc. Am. **47**, 1469–1470 (1970).

[26] A. I. Eller, "Survey of thermal, radiation, and viscous damping of pulsating air bubbles in water," J. Acoust. Soc. Am. **31**, 1654–1667 (1970).

[27] W. H. Press, B. P. Flannery, S. A. Teukolsky, and W. T. Vetterling, *Numerical Recipes in FORTRAN: The Art of Scientific Computing*, 2nd ed. (Cambridge, New York, 1992), Ch. 16.

[28] C. C. Church, "A method to account for acoustic microstreaming when predicting bubble growth rates produced by rectified diffusion," J. Acoust. Soc. Am. **84**, 1758–1764 (1988).

[29] Yu. A. Ilinskii, Program Ma20p documentation, March 28, 2007.

[30] M. Minnaert "On musical air-bubbles and the sound of running water," Philosophical Magazine **16**, 235–248 (1933).

[31] Chief of Naval Operations, "Final Comprehensive Report for the Operation of the Surveillance Towed Array Sensor System Low Frequency Active (SURTASS LFA) Sonar Onboard the R/V Cory Chouest and USNS IMPECCABLE (T-AGOS 23) Under the National Marine Fisheries Service Regulations 50 CFR 216 Subpart Q," U.S. Dept. of Navy, Washington, DC, 100 pages (2007).

[32] W. J. Richardson, B. Würsig, and C. R. Greene, "Reactions of bowhead whales, *Balena mysticetus* to drilling and dredging noise in the Canadian Beaufort Sea," Marine Environ. Res. **29**, 135–160 (1990).

[33] The Washington Post, "Appeals court upholds curbs on Navy's sonar training off Calif.," March 2, 2008, p. A9.

[34] L. Greenhouse, "Justice takes case on navy use of sonar," The New York Times, June 24, 2008.

[35] A. Liptak, "Supreme Court Rules for Navy in Sonar Case," The New York Times, Nov. 12, 2008.

Vita

Adrian Mohamed Larbi-Cherif was born on June 24, 1982 and raised in El Paso, Texas, the son of Said and Linda Larbi-Cherif. He entered The University of Texas at El Paso in 2000, and he received the degree Bachelor of Science in Physics and Bachelor of Science in Applied Mathematics in the year 2005. He was admitted into the Graduate School of The University of Texas at Austin in the fall of 2005.

Permanent address: 301 Bird Avenue
El Paso, Texas 79922

This thesis was typeset with LaTeX[†] by the author.

[†] LaTeX is a document preparation system developed by Leslie Lamport as a special version of Donald Knuth's TeX Program.